M. Tech Thermal Engineering

Vaibhav Singh

2023

Simulation of Stirling Engine

A DISSERTATION

SUBMITTED IN PARTIAL FULFILLMENT OF THE
REQUIREMENTS FOR THE AWARD OF THE DEGREE OF

MASTER OF TECHNOLOGY

IN

THERMAL ENGINEERING

Submitted by:

VAIBHAV SINGH

(2K21/THE/18)

Under the supervision of

Dr. Anil Kumar

Associate Professor

DEPARTMENT OF MECHANICAL ENGINEERING

DELHI TECHNOLOGICAL UNIVERSITY

(Formerly Delhi College of Engineering)

Bawana Road, Delhi-110042

MAY, 2023

DELHI TECHNOLOGICAL UNIVERSITY

(Formerly Delhi College of Engineering)

Bawana Road, Delhi – 110042

CANDIDATE'S DECLARATION

I, VAIBHAV SINGH, 2K21/THE/18, of M. Tech (Thermal Engineering), hereby declare that the project Dissertation titled "Simulation of Stirling Engine" which is submitted by me to the Department of Mechanical Engineering, Delhi Technological University, Delhi in partial fulfilment of the requirement for the award of the degree of Master of Technology, is original and not copied from any source without proper citation. This work has not previously formed the basis for the award of any Degree, Diploma Associateship, Fellowship, or other similar title or recognition.

Place: Delhi **VAIBHAV SINGH**

Date: **(2K21/THE/18)**

DELHI TECHNOLOGICAL UNIVERSITY

(Formerly Delhi College of Engineering)

Bawana Road, Delhi – 110042

CERTIFICATE

I hereby certify that the Project Dissertation titled "Simulation of Stirling Engine" which is submitted by VAIBHAV SINGH, 2K21/THE/18, Department of Mechanical Engineering, Delhi Technological University, Delhi in partial fulfilment of the requirement for the award of the degree of Master of Technology, is a record of the project work carried out by the student under my supervision. To the best of my knowledge, this work has not been submitted in part or full for any Degree or Diploma to this University or elsewhere.

(DR. ANIL KUMAR)
Associate Professor
Department of Mechanical Engineering
Delhi Technological University
Bawana road, Delhi – 110042

ACKNOWLEDGEMENT

I would like to offer my heartfelt appreciation to everyone who helped me finish this academic project. This initiative would not have been feasible without their assistance and support.

First and foremost, I would want to thank **Dr. Anil Kumar** (Delhi Technological University) my academic project supervisor, for leading me through the project and giving me vital insights and criticism. I appreciate the time and work he has put into me. I am also thankful to him for allowing me to work from and providing machine necessary for this work at Center for Energy & Environment, Green Energy Lab, Mechanical Engineering Department.

I would like to thank **Prof. S.K Garg** (Head of the Department, Delhi technological university) and my teachers for motivating and inspiring me throughout this journey, and for their brilliant comments and suggestions.

I also want to thank my family and friends for their constant support and encouragement during this effort. Their faith in me has been both motivating and inspiring.

VAIBHAV SINGH
(2K21/THE/18)

ABSTRACT

In the face of dangers posed by Climate Change in the World today. A shift to renewable sources is the need of the hour. A healthy mix of different energy sources of both renewable & non-renewable nature is the way to move forward. A Solar Stirling Engine has one of the highest thermal efficiency among Solar Thermals. Its applications can play a vital role in contributing to this energy mix of fuel sources. Among the various types of analysis methods for the Stirling Engine, fourth-order analysis, which is Computational Fluid Dynamics (CFD) analysis, is the only one that considers the actual geometry of the engine, and is capable of recognising complex gas flow behaviour, uneven pressure and temperature distributions in the engine. The present work summarises applications of solar Stirling Engine, 2D and 3D CFD simulation studies, list them under the different software such as ANSYS Fluent, OpenFOAM and COMSOL that were used for simulation, highlighting the study type, computational domain and eddy viscosity models used for modelling of Stirling Engine. Hydrogen, Helium and Air are popular working fluids of Stirling Engine, Air being the safest and cheapest working fluid. Studies regarding 3D CFD performance analysis of the Stirling Engine are limited. The work performs a 3D CFD Simulation of the GPU3 Stirling Engine with Air as the working fluid. It was found that there was a reduction in power output and efficiency by 40% and 46% respectively as compared to using helium as working space. The impinging effect was responsible for vortex formations and enhancement of heat transfer.

CONTENTS

NOMENCLATURE

A	Area, m^2
A_{fs}	Interfacial area density. 1/m
a_1,a_2	Friction factor correlation constants, -
a_3,a_4	Nusselt number correlation constants, -
C_2	Inertial resistance coefficient, -
C_f	Friction coefficient, -
C_p	Specific heat
d	Diameter, m
E	Specific energy, J/kg
e	Eccentricity, m
h	Heat transfer coefficient, $W/m^2.K$
K	Thermal conductivity, W/m.K
k	Turbulent kinetic energy, J/kg
L	Length, m
m	Mass, kg
N	Operating speed, rpm
Nu	Nusselt number, -
P	Power, W
p	Pressure, Pa
Pr	Prandtl number, -
$\dot{Q}$	Heat transfer rate, W
$\dot{q}$	Heat flux, W/m^2
R	Gas constant, J/kg.K
R_c	Crank radius, m
Re	Reynolds number, -
S_i	Momentum source term, N/m^3
t	Time, s
T	Temperature, K
u, v, w	Velocity components, m/s
u_r	Relative velocity, m/s
V	Volume, m^3
w	Work, J/cycle
y	Vertical distance, m
y^+	Dimensionless wall distance, -

Greek symbols

1/α	Viscous resistance coefficient, -
A	Thermal diffusivity, m^2/s
γ	Regenerator porosity
Δn	Thickness of porous media
Ɛ	Dissipation rate, m^2/s^3
Ɵ	Crank angle, deg
λ	Bulk viscosity coefficient, Pa.s
μ	Dynamic viscosity, Pa.s
ρ	Density, kg/m^3
ψ	Viscous dissipation, W/m^3

ω	Specific dissipation rate, m^2/s^3
ω_r	Angular frequency, rad/s

Subscripts

b	bore
c	compression
cr	connecting rod
cs	cross-sectional
d	displacer
e	expansion
eff	effective
f	fluid
h	hydraulic
i, j, k	coordinate directions in index notation
ind	indicated
p	piston
r	regenerator
s	solid
t	turbulent
tot	total
w	wire

LIST OF FIGURES

LIST OF TABLES

CHAPTER 1 INTRODUCTION

The world is currently experiencing an energy and resource shortage as the human need for energy has been increasing rapidly and at an alarming rate. To protect scientific and technical progress, numerous organisations have been actively discovering and examining alternate energy sources [1], [2]. Presently, most of our energy comes from oil, coal, gas, and other hydroelectric and renewable energy sources. Oil, coal and natural gas are carbon fuels buried inside the earth's crust but burning them releases all that carbon into the atmosphere, disrupting the balance of gases in the atmosphere. Hence, we can say that the human need for energy is directly responsible for climate change. The way to tackle this is to reduce our energy requirements, and then shift the energy sources from fossil fuel to renewable. This shift to renewable energy should be well planned as manufacturing the energy converters for renewable to usable energy also causes emissions. Therefore, the pacing and mix of energy sources are crucial[3]. A good energy mix of renewable and non-renewable sources is the need of the hour. For this several hybrid systems like combined heat and power systems or grid-connected renewable systems with or without energy storage are being investigated [2], [4].

The Prominent players in renewable energy sources are Wind, Photovoltaics and Solar thermals. Solar thermals include sources like Parabolic Trough Collectors (PTC), Flat plate collectors (FPC), Dish Collectors (DC) & Solar Towers (ST). All these sources can be divided according to the temperature achievable at the collector. FPC can reach up to 100 ºC, PTC up to 400-500 ºC, DC up to 800-1000 ºC and Solar Tower up to 1100 ºC[5]. Thus, low-temperature applications like FPC and PTC are suitable for heating requirements, and high-temperature applications like Dish Collector and Solar Towers for power generation. Out of these, Dish collectors can be modular with high-temperature capability, thus reaching higher efficiencies and yet do not require a large field like for Solar Tower.

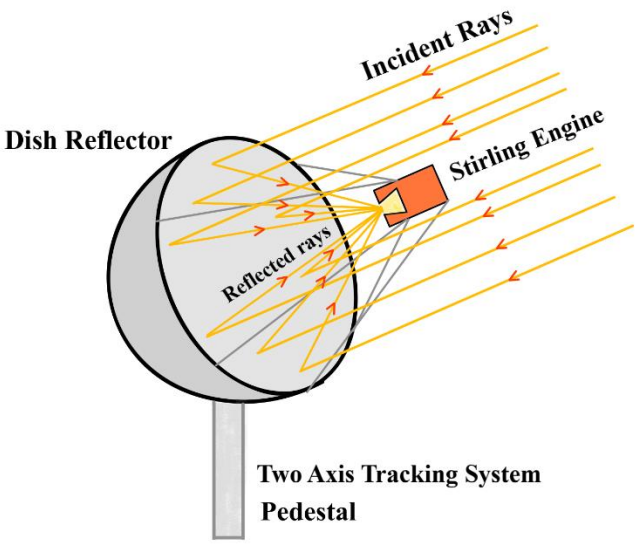

Figure 1.1. Schematic Diagram of a Solar Dish Stirling System

Stirling Engines are external combustion engines, and they operate on the Stirling cycle, a closed regenerative thermodynamic cycle consisting of two isochoric and two isothermal processes. They can operate on fluids like hydrogen, helium, air and nitrogen. Being an external combustion engine, they can operate from various heat sources like Concentrated Solar, Biomass, Geothermal, and fossil fuels[6]. Thus Solar Dish Concentrated System (Fig. 1.1) combined with Stirling engine is an attractive option for power generation with multi-fuel and hybridization capability.[7] Over 200 years ago, since the invention of the Stirling engine, which has a wide range of uses. Since they only have a few moving parts, they have a high efficiency of roughly 35%, little vibration and noise, and straightforward construction. Additionally, Stirling engines can run on environmentally beneficial energy sources like biomass, waste heat, or solar energy [7], [8].

Stirling engines based on solar energy and hybrid systems were investigated by many authors [9]–[15]. Popular applications of solar-based Stirling engine systems include Power Generation, Water pumping, Water distillation, Combined Heat & Power, Off Grid Electrification, Hybridisation, Storage & desalination. Alpha, beta, and gamma-type Stirling engines are the three different types of Stirling engines [16]. Free-piston Stirling engines are those that operate without a piston drive mechanism [16]–[18].

Stirling engines need a thorough thermodynamic analysis for its operation to be understood. Such a study frequently calls for a complex model. Stirling engines are designed and their performance is predicted using five different techniques: zero-order analysis, first-order analysis, second-order analysis, third-order analysis (also known as the nodal design approach), and fourth-order analysis (also known as CFD simulation). In this context, the term "order" refers to classification based on the model's level of complexity, with a higher order indicating a more complex model.

The first-order analysis ignores all losses. The majority of the irreversibilities that are present during the operation of Stirling engines are not taken into account, making this form of study highly straightforward yet unreliable. In the second-order models, calculations are first carried out under the presumption that there are no losses, and once the solution has converged, different forms of losses are estimated independently [19], [20]. These losses include pressure drop, heat exchanger losses, appendix gap losses, conduction and radiation losses, regenerator thermal inefficiency losses, etc. The engine's geometry is discretized in the third-order methods as a network of nodes and control volumes, and a set of differential equations is then solved [21], [22]. The analysis of third-order models is, in general quite complicated and requires more computational effort and time than second-order models[23].

The fourth-order analysis is the CFD analysis, studies have been categorized as either 2D-based or 3D-based and presented under the headings of the software on which they have been conducted. Any Stirling engine type can use the CFD approach because any variation of a parameter is already included in the Navier-Stokes equations. Most accurate analysis can be done by CFD but it also requires the most inputs like an accurate 3D model, and boundary conditions, the selection of appropriate eddy viscosity models and is computationally expensive, i.e. it takes a lot of time for a convergent solution.

CHAPTER 2 LITERATURE REVIEW

2.1 APPLICATIONS OF SOLAR DISH STIRLING ENGINE

Figure 2.1 illustrates the primary uses for solar Stirling engine systems. In this section, recent works about these applications are examined.

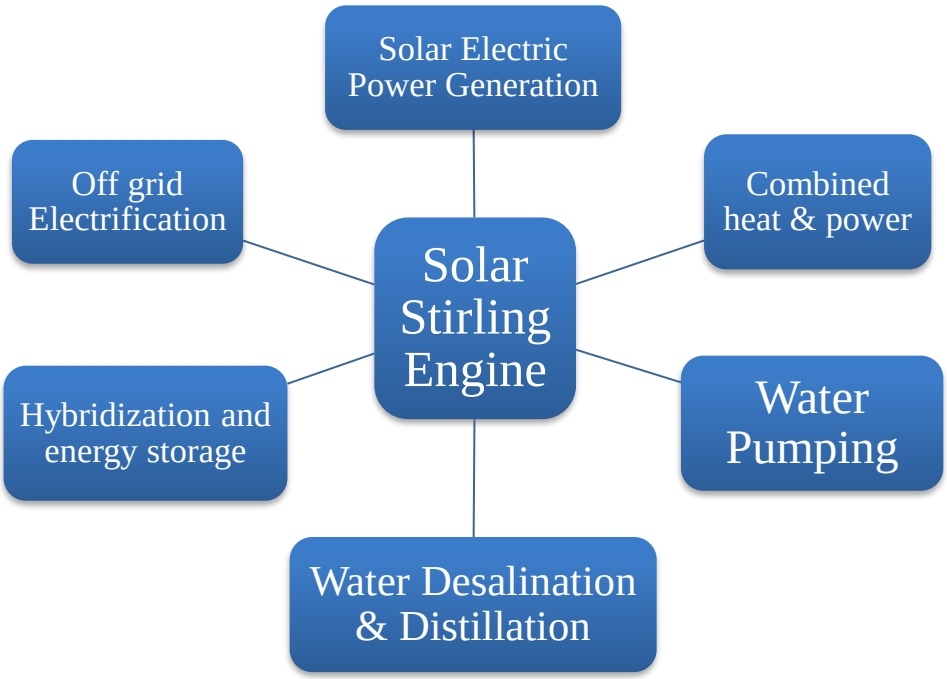

Figure 2.1. Applications of Solar Dish Stirling Engine

2.1.1 Solar Stirling Electric Power Generation

Y. Li, Choi, and Vilathgamuwa[24] created a dynamic model for a solar power plant that allows for temperature variation in the Stirling engine receiver/absorber. Additionally, the capability of the fixed-speed dish-Stirling system to provide frequency control was investigated by varying the operating temperature of the receiver.

Mendoza Castellanos et al.[25] did the experimental analysis and numerical validation of the solar Stirling system with a parabolic dish connected to the electrical grid. The effectiveness of the TRINUM system and the previously published mathematical model showed a variation of 2%–12%. At the Federal University of Itajub, Brazil, the system produced 1 kW of electrical power with a total efficiency of 17.6% at 725 W/m^2 solar radiation.

Lashari et al.[26] used the system advisor model (SAM) to do a techno-economic analysis and power forecast for a 25 kW standalone solar parabolic dish system. The observed DNI is 1719.15 kWh/m^2/year. 38.6 MWh of power can be produced annually by the system, with a net overall efficiency of 23.39%. Because of high insolation, the month of January produced the most energy, 3.38 MWh.

Bidhendi and Abbassi[27] investigated how the PSDS system performed under various operational and meteorological circumstances. It is determined that a 30-degree drop in the temperature of the cold sink will result in a realistic 5% gain in power. With a 24% efficiency, the system will yield its most in desert climates. The production of electric power was 50% lower in humid climates.

Zayed et al.[9] developed, analyzed and optimized a thermodynamically balanced dish Stirling system using multi-objective particle swarm optimization (MOPSO). A sensitivity study was also performed to determine the effects of the rim angle, dish concentrator diameter, and concentrator mirror soiling coefficient. According to sensitivity results, SDSS with concentrator diameters of (2.5–15 m) can provide final ideal output powers of (1.4–33.34 kW) with negligible variations in overall efficiency (29.80–30.20%) at the acquired optimal solutions for the optimized dish concentrator designs. The concentrator's mirror soiling factor, which has a significant impact on the optimal electric power and overall efficiency of SDSS, is also highlighted by the results. Achieving a maximum power of 23.46 kW with an ideal total efficiency of 30.15% is doable with the proposed MOPSO technique.

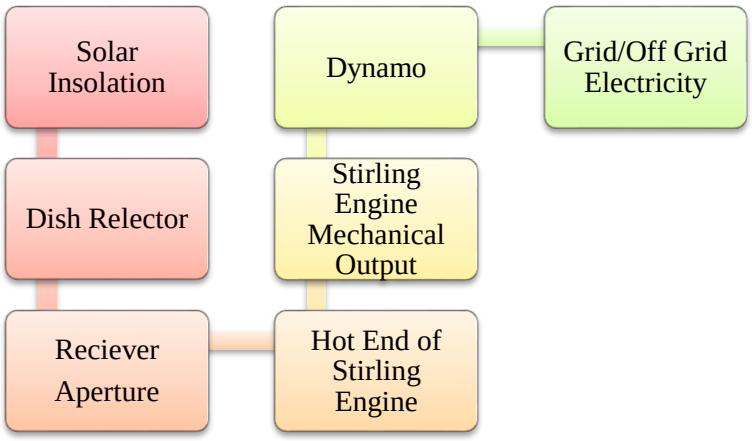

Figure 2.2. Energy flow in a Solar Dish Stirling Engine power plant

2.1.2 Off Grid Electrification

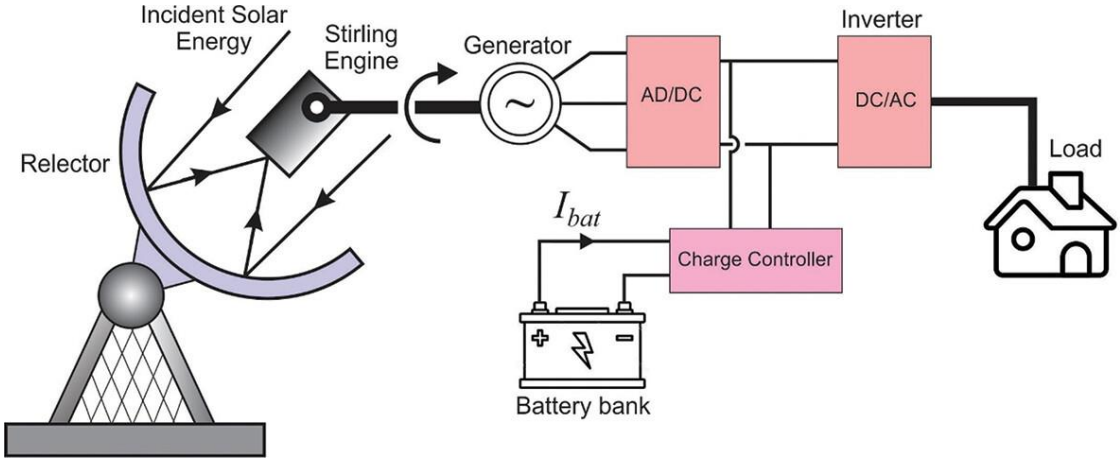

Figure 2.3 Off-Grid electrification dish system [28]

Kadri and Hadj Abdallah[29] assessed the efficiency of a single Stirling solar dish system placed for rural electrification. Simulation studies and thermodynamic modeling were conducted for the Stirling heat engine that runs on solar electricity. To investigate the viability of the hybrid arrangement, a model for a standalone dish-Stirling with PMSG system was created in MATLAB software. A comparison study of the Euro dish system was conducted to validate the model's predictions. Fluctuating speed system was shown to fair option for providing an unmanageable capacity under various climatic circumstances during the cold, moderate, and hot seasons.

In order to electrify rural settlements, Bataineh and Taamneh[28] studied the effectiveness of a standalone PSDS system employing SAM. Results indicated that the Levelized energy cost might be reduced while yearly energy production might increase by 19%. The net overall system efficiency was close to 21%, and under ideal conditions, it may even be increased by 3%.

For a 30 kW small-scale power plant for the electrification of Crowley, Louisiana, Ezeanya et al.[30] established a performance forecasting model in System Advisor Model (SAM). It is possible to reduce the cost of electricity by around 70% by running the power generation plant at the appropriate amalgamation of thermal storage and solar multiple.

The effectiveness of a solar-powered Parabolic Dish Stirling engine for rural electrification in Jordan was assessed[11]. The simulation was carried out in MATLAB software and validated against experimental data with a very excellent match. According

to modeling results, overall system efficiency is predicted to be around 30% in summer and 22% in winter, with 230 being the ideal concentration ratio. Under the varied weather conditions of summer, spring, and fall, storage capacity equal to daily energy consumption was determined to be sufficient to handle the uncontrollable load.

Table 2.1. Recent studies related to Solar Dish Stirling electric generation & off-grid electrification

Author	**Publish year**	**Remarks**
Solar Electric Generation		
Lashari et al.[31]	2020	1. Used the system advisor model (SAM) to do techno-economic analysis and power forecast for a 25 kW standalone solar parabolic dish system. 2. 38.6 MWh of power can be produced annually by the system, with a net overall efficiency of 23.39%. The month of January produced the most energy, 3.38 MWh.
Vahidi Bidhendi and Abbassi [32]	2020	1. Determined that a 30-degree drop in the temperature of the cold sink will result in a realistic 5% gain in power. With a 24% efficiency, the system will yield its most in desert climates. 2. The production of electric power was 50% lower in humid climates.
Zayed et al.[33]	2020	1. Fabricated, studied, and optimized dish Stirling system using MOPSO. 1. SDSS with concentrator diameters of (2.5–15 m) can provide final ideal output powers of

			(1.4–33.34 kW) with negligible variations in overall efficiency (29.80–30.20%) at the acquired optimal solutions for the optimized dish concentrator designs. 2. The concentrator's mirror soiling factor significantly impacts the optimal electric power and overall efficiency of SDSS.
Off-Grid Electrification			
Bataine[34]	2022	1. 2.	The simulation was carried out in MATLAB software and validated against experimental data with a very good match. The overall system efficiency is predicted to be around 30% in summer and 22% in winter, with 230 being the ideal concentration ratio.

2.1.3 Combined Heat & Power

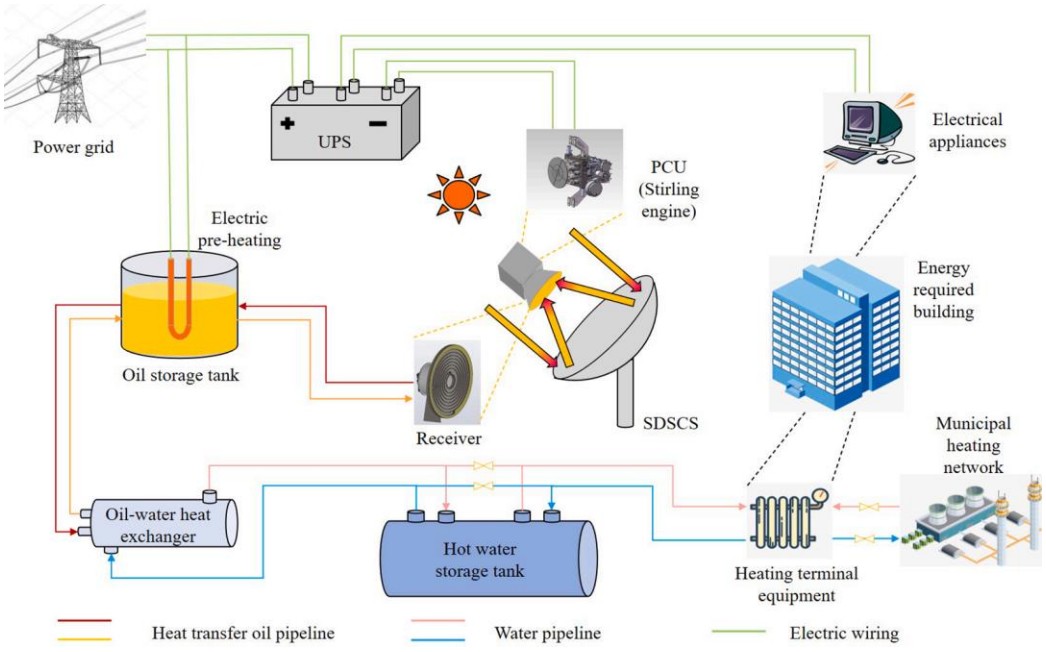

Figure 2.4 Modules and connections in the novel solar dish Stirling cogeneration system[35]

In Forl, Italy, Bianchini et al.[36] conducted an experimental evaluation of the future use of an outdoor 4.5 m diameter dish system for home hot water. They measured the flow rate and temperatures of cooling fluids, receiver temperature, weather data, and power output. The solar dish was discovered to produce heat at a rate of roughly 5440 kWh in 1326 hours. According to reports, the planned solar dish cloud would be utilized in the winter to pre-heat domestic hot water and provide space heating. At the same time, in the summer, it would be suitable for hybridization with an absorption chiller to provide space cooling and produce hot water.

A unique cogeneration system based on Stirling solar dish technology was created by Gu et al.[35]**.** The recommended system has a control strategy that enables switching between heat and power supply utilizing a movable dual receiver. Compared to the normal design, this novel configuration with SDSCS demonstrated superior system running proportion in three different locations in Tianjin, Yinchuan, and Lhasa. A low LCOE power source is also possible with this cogeneration system.

A CFD study of the performance of a solar dish Stirling engine system with micro-cogeneration was conducted by Papurello, Bertino, and Santarelli [37]. COMSOL software was employed. The results showed that a 2.4 m diameter concentrator could generate a value of electrical energy equivalent to 0.99 kWe, starting from 800 W/m^2 of mean irradiance.

2.1.3.1 Building Related

A hybrid system that can deliver energy, cooling, and heating simultaneously was proposed by Açıkkalp, Kandemir, and Ahmadi [38]**.** The system's major components are an absorption refrigeration system, a chemical heat pump, and a solar Stirling engine. The results show that the system performs most effectively at high temperatures for both the collector surface and the operating. The findings indicate that the suggested system, with a maximum power of 9.463 kW, can improve overall energy efficiency by more than 13%.

In order to meet the needs of a hotel building in East Azerbaijan, Iran, for cold, pure water and electricity, Jabari, Nazari-heris, et al.[39]created a novel hybrid design of the PSDS system for cooling, potable water, and power ZEB. The Stirling Engine and evaporator heat exchanger were coupled to a closed-air open-water HDH desalination process via the suggested configuration.

A Dish Stirling photothermal concentrator was created, built, and virtually tested by Merabet, Chouichi, and Kerboua [40] to meet the requirements of a minor housing structure in a coastline city of Algeria outside the solar belt. A 10.52 m-diameter Dish Stirling system was created, utilizing hydrogen as the working fluid and a concentration factor of 1000. It was found to be 23 kW in the month of July during solar noon equating to roughly 153% of the prerequisites of the families being met.

In order to satisfy the electric needs of sustainable multi-family buildings with the potential for clean hydrogen production, Allouhi, Allouhi, Almohammadi [41] proposed and optimized a hybrid renewable energy system based on microgrid power. The proposed hybrid system has a battery bank, an electrolyzer, a hydrogen storage tank, and Solar Dish Stirling (SDS) technology integrated with a wind turbine (WT) for power generation. Results show that the hybrid system design is site dependent. The model's performance was assessed for two cities in Morocco. For Dakhla and Ouarzazate, the optimal HRES design yielded LCOH values of 21.4 and 23.6 euros per kilogram, respectively. This study opens up possibilities for the SDS's use in carbon-neutral buildings and indicates the possibility of its deployment in future HRESs.

Guarino et al.[12] proposed developing a cogeneration plant that would produce heat and electricity by combining dish-stirring collectors with cyclical geothermal storage as well as water-to-water pumping systems. The facility was designed to generate electricity and provide thermal energy for a building's heating system in Palermo. Based on modeling results, it is possible to use solar energy to meet 97% of yearly thermal demands using optimal plant configuration. Other uses are permitted for the residual 64% of the electricity by the electric engines.

2.1.3.2 Refrigeration

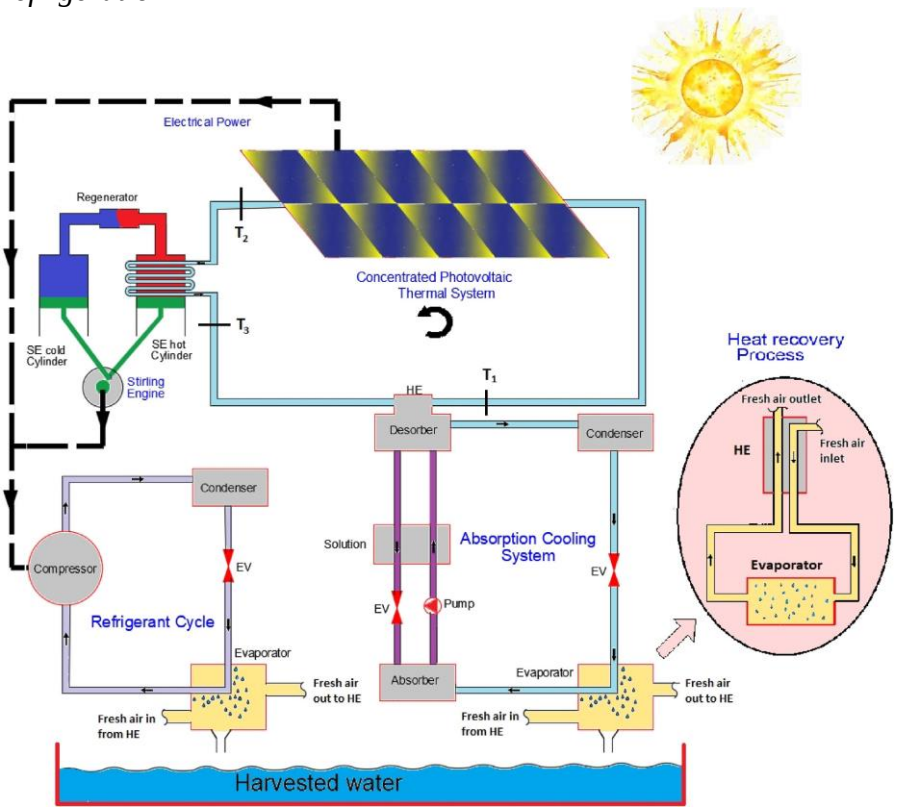

Figure 2.5 hybrid refrigeration & water harvesting system [42]

Al Keyyam et al.[42] looked into the efficiency of a novel integrated solar thermal water harvesting system that uses a CPV/T to harness solar energy and generate electrical energy. An α-type engine and a absorption cooling cycle (single-effect LiBr/H_2O) are powered by rejected heat. The cooling effectiveness is used to chill and remove humidity from surrounding air and produce drinkable water, while the output power and the CPV/T is utilised to run a vapour compression cycle. The highest water production rate, around 30 L/h, was found to occur in hot, humid areas with high radiations from the sun, surrounding temperature as well as humidity. The suggested method is appropriate for small-scale applications with water demands under 180 liters daily. The amount of electrical energy used by this system to create one liter of water is between 225 and 315 Wh/L in general.

Table 2.2. Remarks about Heat & Power Combined

Author	Publish year	Remarks
Combined Heat & Power		
Gu et al.[43]	2021	It has a control strategy that enables switching between heat and power supply utilizing a movable dual receiver. A low LCOE power source is also possible with this type of cogeneration system.
Papurello, Bertino, and Santarelli[44]	2021	A CFD study of the performance of a solar dish Stirling engine system with micro-cogeneration using COMSOL software. A concentrator of 2.4 m diameter could generate a value of electrical energy equivalent to 0.99 kWe, starting from 800 W/m2 of mean irradiance.
Building related		
Merabet, Chouichi, and Kerboua [45]	2022	A 10.52 m-diameter Dish Stirling system was created, utilizing hydrogen as the working fluid and a concentration factor of 1000. It was generating 23 kW in the month of July during noon, equating to roughly 153% of the demands.
Allouhi, Allouhi, Almohammadi, et al.[46]	2022	The proposed hybrid system has a battery bank, an electrolyzer, a hydrogen storage tank, and Solar Dish Stirling (SDS) technology integrated with a wind turbine (WT) for power generation. For two cities of Morocco, Dakhla and Ouarzazate, the optimal HRES design yielded LCOH values of 21.4 and 23.6 euros per kilogram, respectively.

Guarino et al.[47]	2022	A cogeneration plant that would produce both heat and electricity by combining dish-stirring collectors with cyclical geothermal storage as well as water-to-water pumping systems. Using solar energy to meet 97% yearly thermal demands with optimal plant configuration is possible. Other uses are permitted for the residual 64% electricity by the electric engines.
Refrigeration		
Al Keyyam et al.[48]	2021	The highest water production rate, around 30 L/h, was found to occur in hot, humid areas with high solar radiation, ambient temperature, and relative humidity. The amount of electrical energy used by this system to create one liter of water is between 225 and 315 Wh/L in general.

2.1.4 Hybridisation & Storage

In the field of research, the solar dish-Stirling engine is increasingly being combined with thermal energy storing systems or hybridized with other sources which are renewable. Additionally, hybridization makes it possible for the system to operate more continuously. Also, these systems In the field of research, the solar dish-Stirling engine is increasingly being combined with heat energy storing systems or hybridized with other renewable energy sources. Additionally, hybridization makes it possible for the system to operate more continuously. These methods also lessen reliance on solar energy's supply. This section discusses recent research in hybridization and heat energy storing systems combined with dish-Stirling engine.

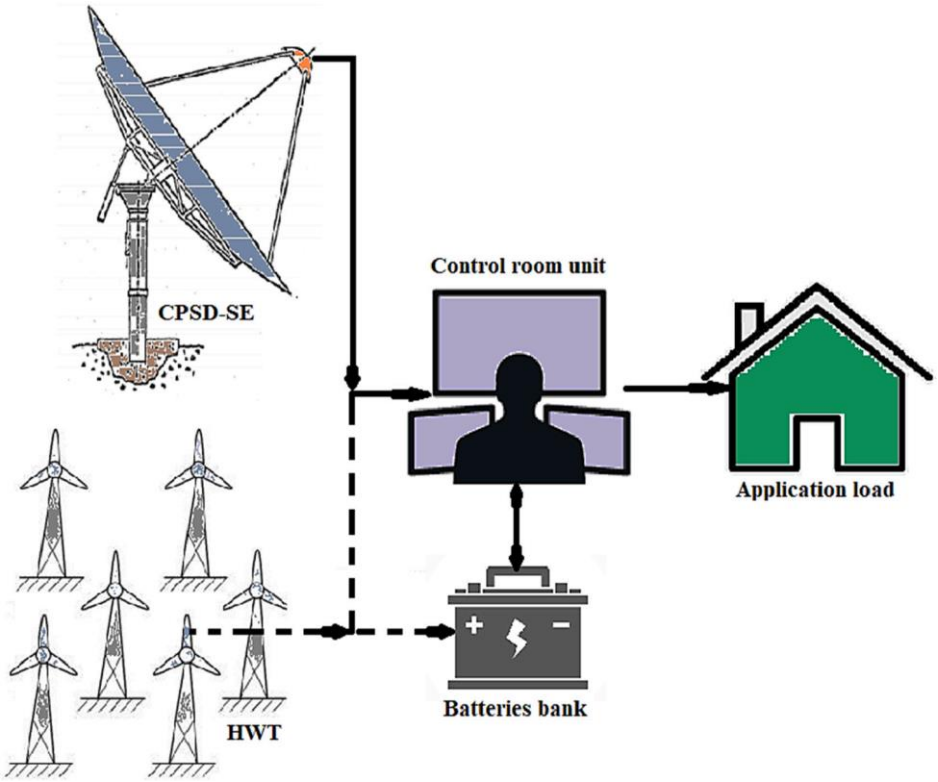

Figure 2.6 New hybrid CPSD-SE/HWT system[13]

Andraka [49] examined the impact on the optimized energy cost after determining whether it was feasible to add thermal storage to a dish-Stirling system. Engine and heat storing units were placed at the rear of the parabolic dish to enhance the configuration. Studies found that a dish-Stirling storing unit could enhance value and significantly lower the life cycle cost of ownership. For ideal value of a solar multiple (1.25) and storage capacity (6 hours), a storage system integrated with a Dish-Stirling can provide value and reduce the Levelized cost of electricity.

To prevent thermal overloading and boost the system's conversion efficiency, Mohammadnia et al.[50]devised a novel hybrid system that combines a Solar Dish Stirling System (SDSS) with a thermoelectric generator (TEG), which serves as an energy harvester. According to reports, the Stirling engine was shielded from unfavorable temperature increases over the critical temperature thanks to the temperature regulation of the cavity using the TEG. This was especially true during the evening and morning hours when solar irradiation was low. At maximum sun irradiation, the projected TEG-SDSS produced 14.1 kW. (solar noon). Furthermore, the temperature management strategy increased the system's overall performance by 20–30%.

A system based on a solar Stirling engine and a diesel engine was proposed by Jabari, Nazari-Heris, et al.[51] The installation of this system aims to meet peak energy demand throughout the summer while assuring clean, reliable and independent power generation. The outcomes of a microgrid reduced the daily cost by 15.4 dollars and the amount of electricity used from the main power supply.

Mehrpooya et al. 2021[52] assessed the effectiveness of a combination system made up of a Stirling engine, a parabolic dish concentrator, and a thermoelectric drive under varied conditions. Stirling Engine exhaust is transmitted to TEG hot end, which generates electricity. The system's performance was assessed for several scenarios and the cities of Moscow, Kiev, Tehran, Beijing, and Geneva.. Additionally, Tehran, Beijing, and Moscow systems have greater justifications for the PDC numbers than the systems in the other two cities (Geneva and Kiev).

Li et al.[53] introduced and demonstrated a brand-new energy system that combines an electrolyzer, a photovoltaic field, an alkaline fuel cell, a Stirling engine, and an absorption chiller. Additionally, they considered a second pumped hydro compressor air system subsystem and assessed them under various working situations. According to the results, a 1 kW(el) AFC produces 1.27 and 2.48 kW of power and cooling load from the Stirling engine and absorption chiller, respectively, with a system efficiency of 63.8%.

A unique hybrid system consisting of a horizontal axis wind turbine and concentrated parabolic solar dish Stirling engine was developed, designed, and technologically and economically evaluated by Shboul et al.[13]**.** The wind turbine (horizontal axis) works with a battery to provide standby power if the prime power source is absent. The efficiency of the Stirling engine is 37% at the optimal design point, with a gross yield power = 1500 kWe. The levelized cost ranges from $0.13 to $0.15 per kWh, and the cost/hour is approximately $4.

2.1.5 Water Pumping

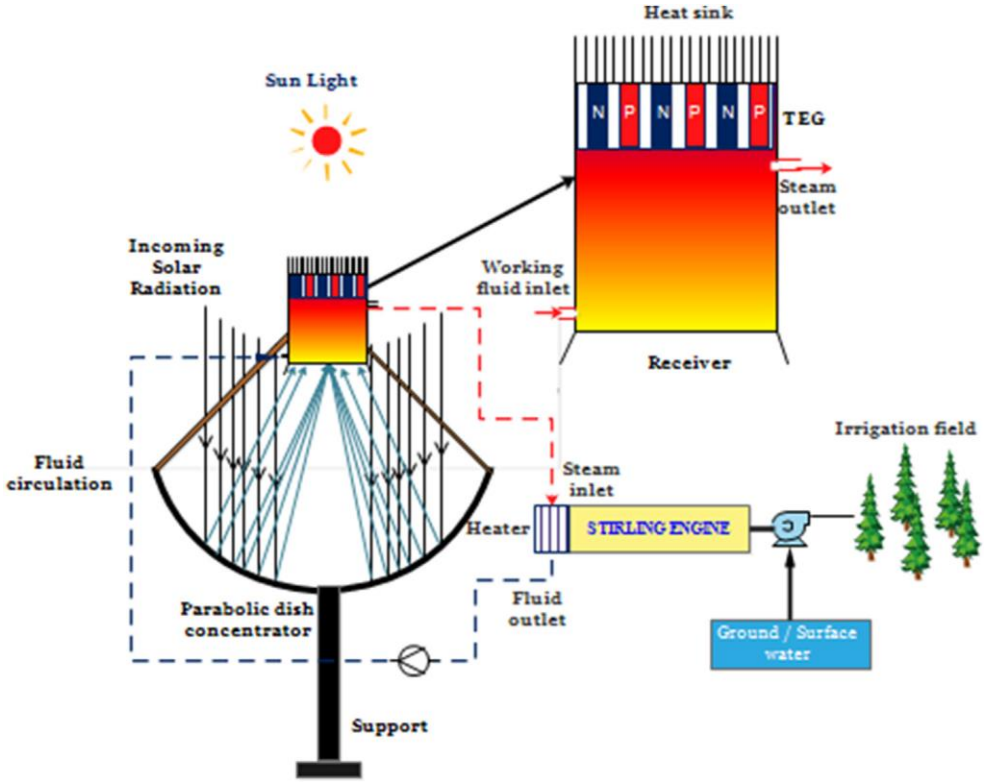

Figure 2.7 Solar dish concentrator coupled with Stirling and TEG [14]

A Stirling converter model that can pump water under various operating conditions was proposed by Tavakolpour-Saleh and Jokar [54]The proposed sophisticated mathematical approach was determined to be inappropriate for the real-time implementation of the model-based controller when they implemented an Artificial Neural Network control system. Thus, a less sophisticated neural network model was proposed; experimental findings supported the viability of the new model.

An innovative Stirling engine design by SunPulse[55] uses air as the operating fluid. A Stirling engine and an incorporated solar heat rotary water pumping syatem were created. The incorporated solar heat technology has the potential use for water pumping in remote or off-grid locations. The market for independent mechanical applications was shown to exist.

Bekele and Ancha [14] examined a small-scale irrigation system for Ethiopia powered by a solar dish Stirling engine. According to the results, the thermoelectric unit produces 5.2 W of electrical power at a maximum efficiency of 2.78% at a heat source temperature of 413.8 K. At a thermal efficiency of 18.61%, the Stirling engine-powered pumping

system delivers a daily aggregate rate of flow = 173,594.95 L. This promotes the nation's food security and enables small farmers to earn more money.

2.1.6 Water Distillation & Desalination

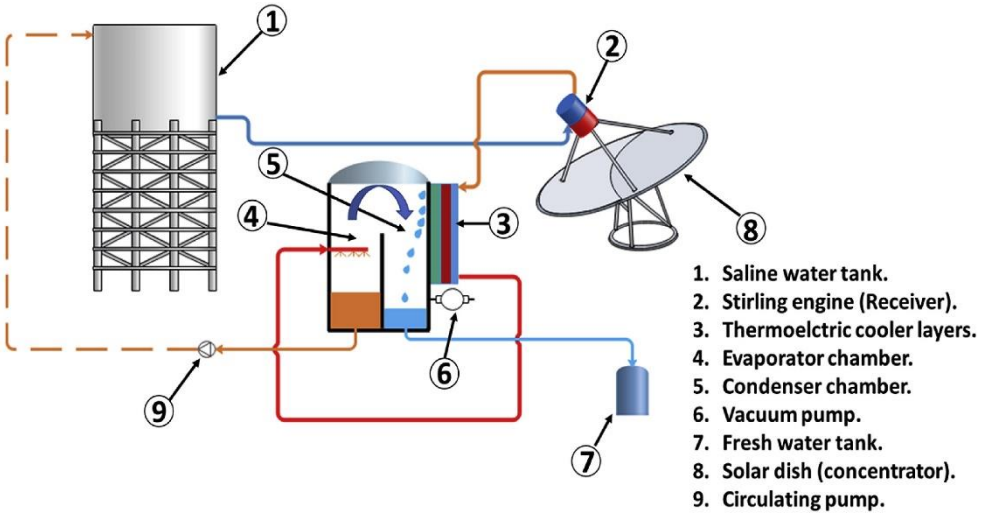

Figure 2.8 CSP based water desalination system [56]

A hybrid energy system was created by Lai et al.[57] that combines an SDSS with an energy storage system based on salinity gradients. To pressurize the seawater into reverse osmosis(RO), the SDSS's generated electricity was used. The ideal operating conditions were chosen to achieve the greatest possible energy efficiency. 9.23% is the highest possible energy conversion efficiency that has been attained.

Al-Nimr and Al-Ammari [56] suggest a cutting-edge solution that combines TEC and Solar Stirling Engine modules. The saline water has been heated using recycled waste heat from the TEC module's hot and SE's cold sides. Additionally, the condensation and water desalination rate was increased using the TEC modules' cold side. As a result, the distillation rate rises to 40.96 kg/day from 2.93 kg/day, and the efficacy rises to 64.44% from 22.84%.

Soliman et al.[58] investigated an innovative wastewater treatment method for Libya's Al-Marj area's industrial sector. The primary power source for operation including reverse osmosis will be a solar Stirling engine. Instead of batteries or diesel generators, a hydraulic power system will be used as an energy storage and recovery system. The outcome show that overall price for was inbetween 0.65 $/m^3, and particular power depletion was not greater than 4 kWh/m^3. The freshwater produced is estimated to supply 55,000 residents.

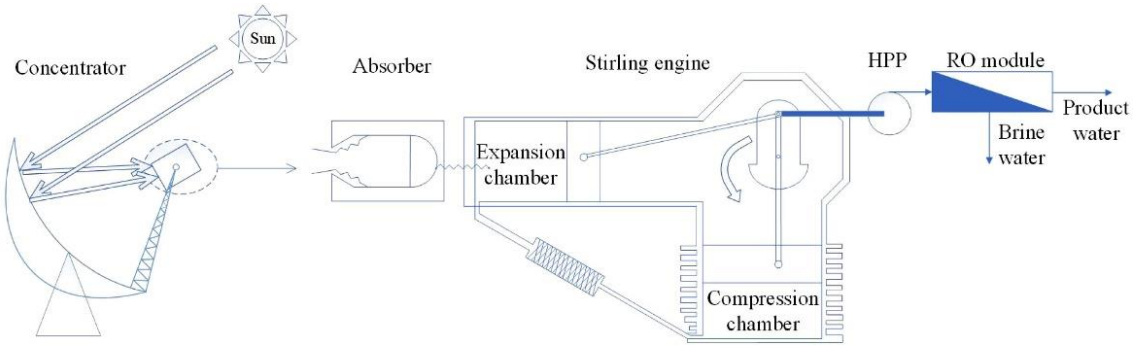

Figure 2.9 Solar DS-powered RO desalination system [15]

A complete parametric study centered around finite-time thermodynamics is conducted to assess the system's water productivity and energy and exergy efficiency. Geng, Cui, and Fan [15] introduced a RO desalination system powered by a solar dish-Stirling (DS) engine. The maximum water productivity, energy/exergy efficiency, and average absorber temperature were shown to be linearly correlated with the source side's ideal working fluid temperature. The water productivity and energy/exergy efficiency first rise with rising sink side temperature before falling.

Table 2.3. Hybridisation & Storage, Water Pumping, Water Distillation & Desalination

Author	Publish year	Remarks
Hybridisation & Storage		
Mehrpooya et al.[59]	2021	A hybrid system comprises a Stirling engine, a parabolic dish concentrator, and a thermoelectric drive under varied conditions. Stirling Engine exhaust is transmitted to TEG hot end, which generates electricity.
Li et al.[60]	2021	A hybrid system that combines an electrolyzer, a photovoltaic field, an alkaline fuel cell, a Stirling engine, and an absorption chiller. 1 kW(el) AFC produces 1.27 and 2.48 kW of power and cooling load from the Stirling engine and absorption chiller, respectively, with a system efficiency of 63.8%.
Shboul et al.[61]	2021	Hybrid system consisting of a horizontal axis wind turbine and concentrated parabolic solar dish Stirling engine. The wind turbine (horizontal axis) works in tandem with battery source to provide standby power if prime source of power is absent. The efficiency of the Stirling engine is 37% at the optimal design point, with a net output power of 1500 kWe. The Levelized cost of energy is found to be between $0.13 and $0.15 per kWh.
Water pumping		
Bekele and Ancha [62]	2022	Small-scale irrigation system for Ethiopia powered by a solar dish stirling engine.

		The thermoelectric unit produces 5.2 W of electrical power at a maximum efficiency of 2.78% at a heat source temperature of 413.8 K. At a thermal efficiency of 18.61%, the Stirling engine-powered pumping system delivers a daily aggregate 173,594.95 L rate of flow.
Water distillation & desalination		
Geng, Cui, and Fan [63]	2021	A RO desalination system powered by a solar dish-Stirling engine. The maximum water productivity, energy/exergy efficiency, and average absorber temperature were shown to be linearly correlated with the source side's ideal working fluid temperature.

2.2 Simulation Modelling of Stirling Engine

ANSYS Fluent is a general-purpose industry-leading computational fluid dynamics (CFD) programme used to model fluid flow, heat and mass transfer, chemical processes, and more. It is renowned for its extensive physics modelling capabilities and industry-leading accuracy [64].

A finite element analysis, solver, and simulation software package called COMSOL Multiphysics are used for a variety of physics and engineering applications, particularly coupled phenomena and Multiphysics. The programme supports coupled systems of partial differential equations and standard physics-based user interfaces [65].

An open-source C++ toolbox called OpenFOAM (short for "Open-source Field Operation And Manipulation") is used to create customised numerical solvers and pre- and post-processing tools for continuum mechanics problems, most notably those involving computational fluid dynamics (CFD) [66].

2.2.1 2D-based studies

2.2.1.1 Custom codes

Mahkamov[67], in 2006, conducted a two-dimensional axisymmetric computational fluid dynamic study for the working process of an alpha-type Solar Stirling Engine. The standard k-ε turbulence model was used, and results were validated which indicated an error of approximately 40%in power prediction. Even though the error is huge, it was significantly better than the power predicted by lower-order methods. This is attributed to the fact that CFD represents the complexities of fluid flow and temperature variation better than second-order methods. According to Makhmov, for layouts other than alpha, the axisymmetric calculation scheme will provide only a preliminary estimation of the engine performance. Three-dimensional CFD is preferred for accurate results.

Salazar and Chen [68] used their own compressible flow CFD code to research a straightforward beta-type engine. Due to the low engine speed, the fluid flow was considered to be laminar when the computer model was built in an axisymmetric and 2D domain. The engine was of low power with no external regenerator. Study suggested that flow impingement was responsible for the majority of thermal transmission and at any given moment, heat dispersal is exceedingly uneven throughout the engine.

2.2.1.2 COMSOL

Alfarawi et al. [69] used CFD simulation to investigate how the phase angle and dead volume affected a gamma-type engine. The fluid flow was regarded as laminar, and the Lagrangian-Eulerian (ALE) technique was used to manage moving engine components and changing cylinder volume. One of the most effective strategies to regulate Stirling engine output is considered to be changing phase angle. Phase angle affects three key engine parameters: pressure amplitude, total volumetric change of gas, and heat transfer, all of which have a direct impact on the engine's indicated power.

2.2.1.3 Open FOAM

In the study of Della Torre et al. [29], a 2D axisymmetric beta-type Stirling engine simulation was performed using OpenFOAM open-source software employing an experimental model created by the France University of Valenciennes. The engine was first parametrically analysed before simulation findings were assessed using experimental data. In the parametric study, the effects of engine power output and engine thermal efficiency were assessed for the kind of working fluid, regenerator characteristics, average engine pressure, and heat received by the engine.

OpenFOAM, an open-source program, was used to model a beta-type Stirling Engine by Mohammadi and Jafarian [70]. The GPU-3 Stirling engine's CFD model with laminar flows produces results that are less than 1% different from those produced by the k-SST turbulence model, indicating that laminar flow is predominant. The average pressure is 1.5 bars, and the power output is 13.2W. A 2D model of the engine's complex shape was oversimplified, and numerous assumptions were made without taking into account mechanical friction, shuttle effects, mass leakages, or regenerator inefficiency. As a result, the regenerator's actual flow characteristics and the intricacy of the heat transfer mechanism between solid and fluid are disregarded.

2.2.1.4 ANSYS Fluent

Ben Mensour et al.[18] performed a CFD analysis of a Stirling engine by considering internal radiation, which is neglected by most researchers. The charge Pressure of the engine was atmospheric with no external regenerator and laminar flow is assumed. The largest discrepancy between the CFD model's predictions and the experimental data was 7%. The absence of radiative heat transfer led to a 13% underestimating of power production. The inaccuracy in estimating power output reached 18% when the cumulative effects of radiation were disregarded. The Discrete Ordinates (DO) radiation model was

found to provide more accurate results and is less computational expense than the surface-to-surface (S2S) radiation model. The working fluid can also have an impact on internal radiation heat transfer.

In a numerical study, Abuelyamen [71] compared the energy efficiency and power output for 3 different kinds of Stirling engines (α, β and γ). Internal radiation heat transmission within the Stirling engine was taken into account. The three Stirling engine variants did not include regenerators. A set of experimental data from the literature was used to validate the model. The annular connecting pipe was added to the α type Stirling engine in place of the circular pipe because the narrow channel results in a high heat transfer rate. After that, there was an increase in power output (from 0.9 W to 9.856 W) and thermal efficiency (from 1.8% to 10.5%). It was found that vortices are the responsible for good mixing of gas which in turn leads to lower cold space temperature, which reduces the compression work, hence increasing the power output and efficiency. 2D CFD studies performed on Stirling Engines are summerised in Table 2.4.

Table 2.4 Summary of 2D CFD studies performed on Stirling Engines

Author	**Year**	**Engine Type**	**Model used**	**Domain**	**Software used**	**Remarks**
Mahkamov [67]	2006	Alpha	Standard k-ε turbulence	Axis symmetric	Custom	• Over prediction by 0.5kW, approx. 40% deviation. • Heat flux produced by the parabolic concentrator is not uniform on the receiver surface.
Salazar, Chen[68]	2014	Beta		Axis symmetric	Custom	• The assumption of uniform chamber temperatures and the constant heat transfer coefficients to account for heat transfer is too crude to reflect reality.
Alfarawi et al. [69]	2016	Gamma	Laminar	Planar	COMSOL	• Studied the influence of phase angle and dead volume. • Max deviation in indicated power was 9%.
Della Torre [72]	2014	Beta	k-ω	Axis Symmetric	OpenFOAM	• The ideal cycle is significantly • Larger than the real cycle, on a PV graph.

						• Power output of the real cycle is 22% of the ideal cycle
Mohammadi [70]	2018	Beta	k-ω SST turbulence	Axis Symmetric	OpenFOAM	• 15.1% difference as compared to experimental results.
Ben-Mansour et al. [18]	2017	Beta	Laminar	Axis Symmetric	Ansys Fluent	• Considered internal radiation heat transfer. • DO radiation models are better than S2S. • Deviation of 7% with experimental results. • Deviation of 18% when radiation effects in total were ignored.
Abuelyamen[71]	2018	Alpha, Beta & Gamma	Laminar	Axis Symmetric	Ansys Fluent	• Compared performance between alpha, beta and gamma types of Stirling Engines, with no external regenerators. • Considered internal radiation heat transfer. • Gamma(9.223W and 9.8%) has highest Power Output efficiency followed by Beta(8.634W and 7.5%) and Aplha(0.908W and 1.8%). Upon modification, Alpha became the highest(9.856W and 10.5%).

2.2.2 3D-based studies

2.2.2.1 Custom

Chen et al. [73] advanced a three dimensional in-house computational code to simulate the thermal transmission of one-fourth of the domain of a simple low-temperature difference γ-type Stirling Engine. Mechanical friction and thermal radiation were not considered. There was no external regenerator and the power produced is low (0.62W) with low efficiency (4.82%), primarily due to Low-temperature Difference b/w Hot and

Cold Ends and low engine speed. As a result, the assumption of uniform temperature in the chambers and the use of constant heat transfer coefficients was not recommended.

2.2.2.2 COMSOL

Almajri et al. [74] executed a three dimensional simulation of a representative α-type Stirling converter employing COMSOL. Fluctuating working parameters and configurations were analysed. Power output increased by 65% (from 146W to 240W) when the optimised new design parameters and operating conditions were applied.

2.2.2.3 ANSYS Fluent

Mahkamov [75], in 2006, performed the first successful 3D CFD simulation of a Gamma type Stirling Engine run by biomass. Compared to 30% for the second-order results, the forecasts were only 12–18% off from the experimental data. k-ε turbulence model was used and remeshing was accomplished by adding or removing cell layers above the displacer and power piston during the strokes. The results showed that, despite identical shapes, the velocity field varied dramatically between tubes. These variations could result in a highly uneven thermal load on the heater's components and ineffective operation. Additionally, it was shown that while the mechanical efficiency of harmonic engines is greater than that of a discontinuous drive, the thermodynamic efficiency of engines with harmonic piston displacement is lower than that of an ideal Stirling engine. The high amount of pressure drop in the regenerator, the "dead" zone of the compression space, and the trapping of the gas in the pipe bridging the two halves of the compression space were the causes of the original engine's low power output.

A small-size alpha-type Stirling engine was modelled in three dimensions by Li [76] using Ansys Fluent. Along with pressure drop and heat exchange rate in the regenerator, engine performance under various hot heat exchanger and regenerator geometries was assessed. When the findings were compared to experimental data, it became evident that regular-shaped microchannels outperformed wire mesh as a regenerator.

Cheng and Chen [76] studied the impact of different working parameters on a 1 kW β-type Stirling Engine. The parameters included filling pressure, heating temperature, and regenerator porosity. The relative performance of helium, nitrogen and air was also studied and it was found that helium leads to the highest engine performance and nitrogen is better than air. The trend of the numerical predictions agreed with that of the experiment data closely, but the actual values differ by over 27%. Even though some assumptions were good, the study failed to accurately predict the output of the engine.

When Xiao et al. [77] used CFD simulation to investigate the operating parameters of a beta-type Stirling engine, the largest divergence was 13.4%. These variables included wire diameter, matrix mesh, regenerator length, and heat exchanger tube diameter. Redesigned heat exchangers resulted in a 40% increase in calculated power output. Some assumptions were not good, which might lead to inaccuracies like simplified geometry, excessive solid parts, thickness layers and regenerator with perfect regeneration. Effects of Thermal radiation and mechanical friction were also ignored. The dead volume of heat exchangers was significantly reduced in the optimised model, increasing thermal efficiency and output power with little flow resistance loss. It has been observed that more dead space causes the pressure to phase shift.

In his research, Kuban [78] looked at the effects of initial charge pressure, engine speed, and heater temperature on the engine's flow, heat transfer, and indicated power characteristics. They used dynamic meshing and re-meshing techniques in their study to explain how the compression piston and expansion piston moved, and the results showed good agreement with the experimental ones. The author suggests that because they have a major impact on the flow field, whole engines should be taken into account for CFD rather than quarter engines. The k-ε turbulence model is realistic. As rotational speed increases, there are less and smaller differences between the k-w-SST and s-ε realisable models; the k-ε realisable model predicts more. The differences between the k-w-SST and s- ε realisable models are minimal and get less as the rotational speed rises, whereas the k-ε realisable model predicts more. However, in the simulation, the engine's frequencies were set to 3 Hz, 6 Hz, and 10 Hz, respectively, which are slightly low compared to the Stirling cycle's actual process. Additionally, the cooler and heater's CFD models assumed isothermal behaviour.

Schmidt's model and a steady-state CFD simulation were combined, according to Caetano's [79] proposal, to produce the beginning and boundary conditions for a numerical study of a Stirling engine of the kind. The author also emphasises that while CFD models are more accurate and reliable, they nevertheless require input data that is challenging to gather experimentally. The technique not only resulted in a sizable reduction in computing time but also improved the precision of the suggested power forecast. The author draws attention to the adoption of a CFD model that, despite requiring significant computer resources, is more reliable and the fact that there is no clear

methodology in literature to calculate the displacer's temperature profile and neither to extrapolate the initial conditions.

With a detailed geometry of the real engine, El-Ghafour et al. [80] presented a 3D-CFD simulation on the GPU-3 Stirling engine. Six turbulent models were used to simulate the engine and compared against the experimental data, realizable k-ε model with enhanced wall treatment was found to provide the most accurate result, around a 4% difference. Because of encroaching influence of tumble vortices produced by the jetting of flow, the major heat transfer rates within the compression and expansion areas happen during the expansion strokes. However, their research did not take into account the complex conjugate heat transfer of the coupling solid-fluid domain in the porous media regenerator and cold heat exchanger, which may have resulted in some inaccuracy in the heat transfer prediction. The initial temperature parameters for the heater, cooler, and regenerator were set at these temperatures without taking this into account.

Rogdakis et al. [21] verified a 3D CFD model of a β-type Stirling engine, with a validated 1D third-order model. The simulated engine is similar but not identical to the GPU-3 Stirling engine. The 3D model predicted 6.93 kW power and 37% efficiency.

Cheng [81] conducted a CFD parametric study on a 100W Stirling engine and validated it with an experiment. In contrast to the previous conventional k-ε model, they adjusted the rotation speed, charge pressure, heating and cooling temperatures, and piston length. The simulation findings demonstrate that the indicated power (or charged pressure) is linearly related to the total mass. Furthermore, while the charged pressure is relatively low, the thermal efficiency increases. The thermal efficiency decreases when the charged pressure rises above its critical value because the rate of heat input increases faster than the indicated power in the high charged pressure domain.

A Free-Piston Gamma Stirling Engine was subjected to multidimensional CFD modelling by Zhao et al. [82], which was compared with numerical modelling carried out using Sage software. The pressure drop in the cold heat exchanger was found to differ by 10.43%, and the temperature profile of the solid matrix in the regenerator is almost linear in the axial flow direction. The majority of the engine's components were created via additive manufacturing. The advanced free-piston engine's oscillating flow and heat transfer are presumed to be transient, compressible, turbulent, and non-isothermal in this study.

Cheng [84] proposed a novel method for exchanging data between a 2nd order thermodynamic model and a 3D CFD model, which drastically reduced the simulation time. The study was conducted on a 100 W beta Stirling engine with an external regenerator and also validated against the experimental data. A realizable k-ε turbulence model is used. It was discovered that the regenerator takes a lot longer than other chambers to reach the temperature of the solid matrix and the working fluid. After starting CFD with an initial estimate, data is recorded and transferred to a thermodynamic model after a few cycles, and when the discrepancy between the two models' stated power and thermal efficiency is less than 3%, subchamber temperatures and pressure are used to update the CFD model. This advances the model into a stable regime quickly. Cost in CFD is significantly reduced from 227hrs to 80hrs by this method. 3D CFD studies performed on Stirling Engines are summerised in Table2.5.

Table 2.5 Summary of 3D CFD studies performed on Stirling Engines

Author	**Year**	**Engine Type**	**Model used**	**Domain**	**Software used**	**Remarks**
Chen [73]	2014	Gamma	Laminar	Quarter-scaled down to half	Custom	• Studied a Low-temperature difference engine, which had no external regenerator. • Power of engine is 0.62W and efficiency is 4.82%.
Almajri et al.[74]	2017	Alpha	Laminar	Full	COMSOL	• Performed 3D CFD parametric study. • Power output increased by 65%, from 146W to 240W
Mahkamov[75]	2006	Gamma	k-ε Turbulence	Full	Ansys Fluent	• Study of a biomass-powered Stirling Engine. • Deviation for pressure and temperature is between 12% to 18% .
Li et al. [83]	2014	Alpha	Laminar	Full	Ansys Fluent	• Evaluated performance for different hot heat exchangers and regenerator geometries. • Regular-shaped microchannels are better

						than wire mesh regenerators.
Cheng, Chen [76]	2017	Beta	Standard k-ε Turbulence	Full	Ansys Fluent	• Trend of numerical predictions agrees well with experimental data. • Actual values differ by over 27%.
Xiao et al.[77]	2017	Beta	Standard k-ε Turbulence	Simplified	Ansys Fluent	• A maximum deviation of 13.4% with experimental data. • Optimised design had lower dead space with low flow resistance loss, increasing the power output by 40%.
Kuban [78]	2018	Alpha	Realizable k-ε Turbulence	Half	Ansys Fluent	• Realizable version of the k-ε turbulence model, as compared to the standard, has the superior ability to capture the complex flow structures involving separation, rotation and even recirculation regions. • Helium is better than Nitrogen and Nitrogen is better than air as the working fluid.
Caetano et al,[79]	2019	Beta	k-ω SST	Half	Ansys Fluent	• Proposed a combination of Schmidt's model and CFD simulation for quicker simulation of the Engine.
El-Ghafour et al.[80]	2019	Beta	Realizable k-ε EWT	One eighth	Ansys Fluent	• Compared 6 different eddy viscosity models for simulation. • Realizable k- ε model with Enhanced wall treatment (EWT) provides the most accurate results. • Average deviation is 4% compared to experimental data.
Rogdakis et al. [21]	2019	Beta	Standard k-ε Turbulence	One eighth	Ansys Fluent	• Compared validated 1D third order method with CFD method. • Deviation of about 2% in Engine efficiency

						compared to experimental data.
Cheng et al.[81]	2020	Beta	Realizable k-ε Turbulence	Full	Ansys Fluent	• Maximum thermal efficiency of the engine was 41.9% at 10 bar charge pressure.
Zhao et al.[82]	2021	Free piston Gamma	Realizable k-ε Turbulence	One fifteenth	Ansys Fluent	• Compared CFD modelling of Free Piston Gamma Stirling with, numerical modelling done on Sage Software. • Deviation of 10.43% was noted between them. • Direct Numerical Simulation (DNS) and Large Eddy Simulation (LES) can provide more accurate results than Reynolds-Averaged Navier-Stokes (RANS) method. • But it is difficult to use them in complex engineering problems therefore RANS is used.
Cheng at al.[84]	2021	Beta	Realizable k-ε Turbulence	Full	Ansys Fluent	• Proposed a novel method to exchange data between the second-order thermodynamic model and 3D CFD model, to reduce the simulation time. • CFD simulation time reduced from 227 hrs to 80 hrs (~184% reduction).

Regenerator is a critical component of a Stirling Engine, it has an impact on temperature distribution and heat transfer. The local Thermal Non Equilibrium model (LTNE) is important for the accurate modelling of porous regenerators and the radiation model is important for the accuracy of studies of the medium to high-temperature Stirling Engine. But Ansys Fluent has a limitation regarding the simultaneous use of the Porous media Local Non-Equilibrium Model (LTNE) with the Radiation model. Standard radiation models like Discrete Ordinates and Surface to Surface cannot be used with LTNE whereas models like Discrete Transfer Radiation Model and Monte Carlo Ray

Tracing Method can be used with LTNE [85]. This might impact the accuracy of simulation studies involving porous regenerators and studies involving solar energy.

2.3 Commercial Solar Stirling Engine Power Plants

Currently, there are no active utility commercial solar Stirling engine power plants operating in the World. 1.5MW Maricopa Solar was the Largest. A list of Commercial Solar Stirling Engine Power Plants is given in Table 2.6.

Table 2.6. Commercial Solar Dish Stirling Power Plants with details [7], [86]

S No.	**1**	**2**	**3**	**4**	**5**	**6**	**7**
Plant	SAIC/STM	SBP	SES	WGA off grid	Kerman Pilot paraboli c Dish-Stirling System	Maricop a Solar Project CSP project	Tooele Army Depot CSP Project
Location	Salt River Project near phoenix, Arizona, USA	Platafor ma Solar de Almeria (PSA), Spain	Boeing, Huntington Beach, California, USA	Sandia's National Solar Thermal Test Facility, Albuquerqu e, USA	Kerman City, Iran	Peoria, Arizona , United States	Tooele, Tooele County, Utah, United States
Year of installation	1997	2001	2002	2000	2017	2010	2012
Avg daily solar Radiation (kWh/m^2)	6.57	5.2	7.1	6.48	5.48	-	-
Aperture Diameter (cm)	38	15	20	14	12	-	-
Projected Area (m^2)	113.5	56.7	87.7	41.2	-	-	-
Focal Length (m)	12	4.5	7.45	5.45	-	-	-
Type of Engine	STM 4-120 double acting kinematic	SOLO 161 Kinema tic	Kockums/SE S 4-95 Kinematic	SOLO 161 Kinematic	Free Piston Stirling Engine	-	-

Working Fluid	Hydrogen	Helium	Hydrogen	Hydrogen	Helium	-	Helium
Displacement (cc)	480	160	380	160	-	-	-
No of cylinders	4	2	4	2	-	-	-
Operational Speed (RPM)	2200	1500	1800	1800-1890	-	-	-
Control Method	Variable Stroke	Variable Pressure	Variable Pressure	Variable Pressure	-	-	-
Peak Output (kW)	22.9	8.5	25.3	8	0.63	1.5 MW plant output	1.5 MW plant output
Peak Efficiency (%)	20	19	29.4	22.5	17		
Misc. Remarks		Maximum Pressure is 150bars and working temp 650 ºC				60* 25kW dish receivers	429 * 3.5 kW dish receivers

2.4 Research Gap & Objective

From the literature review, it is evident that the integration of the Stirling Engine in hybrid systems as well as standalone systems can contribute to the energy mix for heat and power generation. The Stirling Engine analysis is highly sensitive to its geometry owing to its complex fluid flow, which can only be performed via 3D- Computational Fluid Dynamics (CFD) analysis. Hydrogen, Helium and Air are popular working fluids of Stirling Engine, Air being the safest and cheapest working fluid. Studies regarding 3D CFD performance analysis of Stirling Engine are limited, with no study being performed with air as a working fluid.

The objective of this research is to perform a 3-D CFD Simulation of the GPU3 Stirling Engine with Air as the working fluid.

CHAPTER 3 METHODOLOGY

3.1 Engine Geometry and operating conditions

The GPU-3 engine has a rhombic driving system, sliding rod seals, and a single-cylinder, β-type design. General Motors Research Laboratories initially constructed this engine in 1965 for the American Army [18]. Later, it was transformed into a research configuration by the NASA Lewis Research Centre. Fig. shows an isometric cut section view of the GPU-3 Stirling engine's fluid domain and displacer cylinder.

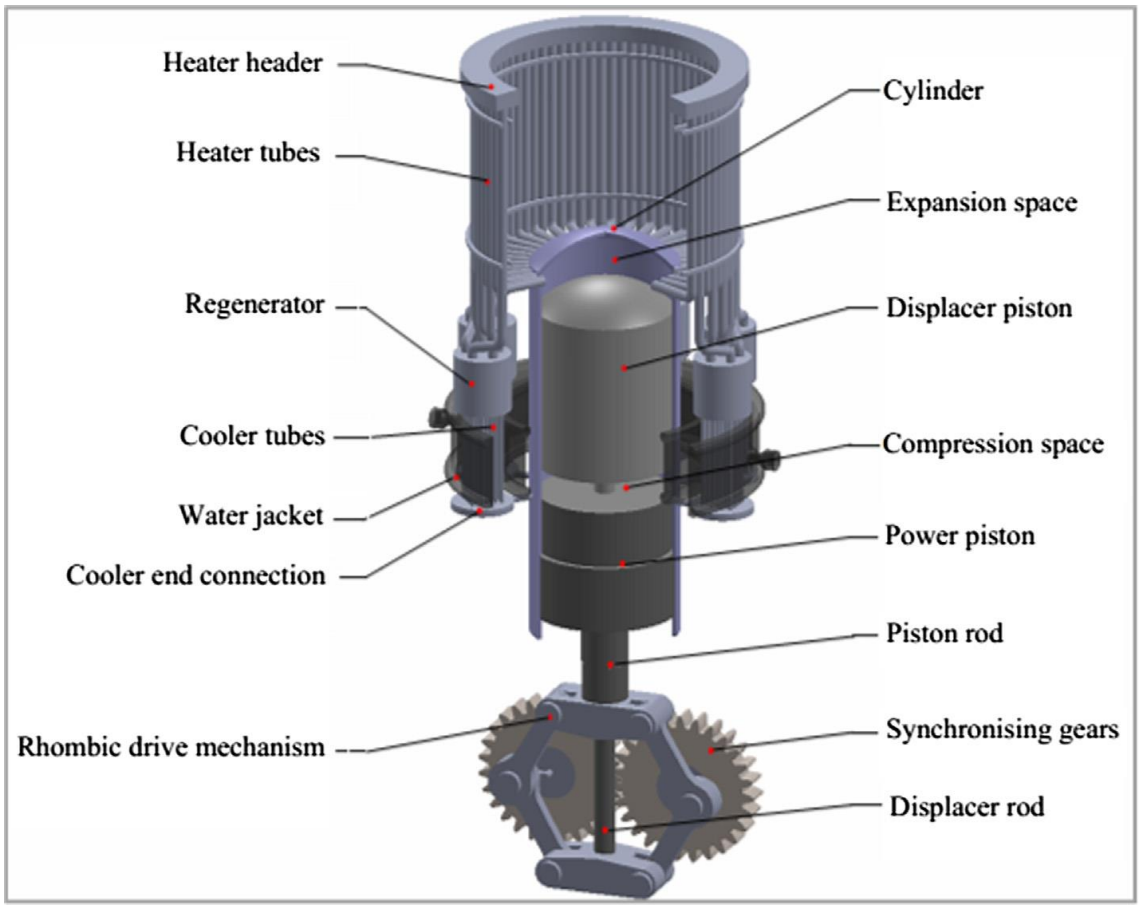

Figure 3.1 Isometric view of GPU-3 Stirling Engine

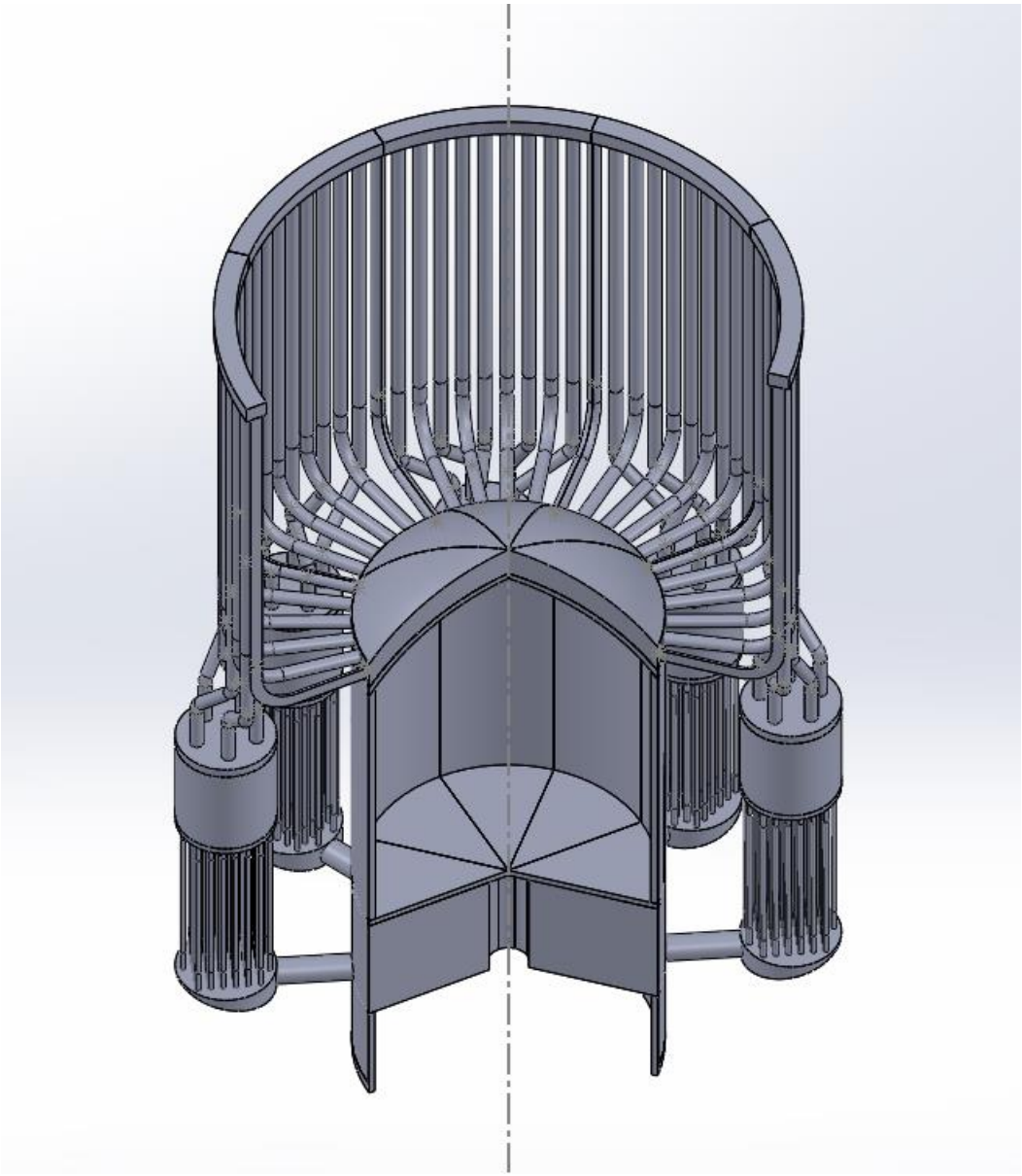

Figure 3.2 Fluid domain from the GPU-3 Stirling engine

The main components of the engine are the cylinder, regenerator, cooler, cooler-end connector, power piston, displacer piston, heater, and rhombic driving mechanism. The power and displacer pistons are arranged concentrically inside the cylinder. The displacer goes up and down utilizing the same drive mechanism as the piston but at a predetermined phase angle since it is connected to a rod that passes through the piston. The compression and expansion spaces are created inside the cylinder by the displacer. The heater, regenerator, and chiller are fixed to the cylinder.

Table 3.1 Design specifications of the GPU-3 Stirling engine, units in cm

Cylinder contents		**Cooler**	
Cylinder bore at liner (db)	6.99	Tube length	4.61
Displacer outer diameter	6.96	Length exposed to cooling water	3.55
	0.15		0.10
Displacer wall thickness	9	Tube inner diameter	8
Displacer total length (Ld)	9.04	Number of tubes per regenerator	39
Displacer and piston stroke	3.12	**Cooler end connection**	
	6.44		
Piston top diameter	8	Connecting duct length	1.59
	5.87	Connecting duct inner	0.59
Piston total length (Lp)	6	diameter	7
Height from gears center to cylinder top wall (Ltot)	31.19	Cooler end caps volume (cm3)	2.77
Heater		**Drive mechanism**	
	11.64	Connecting rod (link)length	
Tube length (cylinder side)	4	(L)	4.6
	12.89		
Tube length (regenerator side)		Crank radius (Rc)	1.38
Length exposed to heat source	7.77	Eccentricity (e)	2.08
	0.30		
Tube inside diameter	2	Piston rod length (Lpcr)	9.33
Number of tubes per regenerator	5	Displacer rod length (Ldcr)	24.4
Regenerator			
Housing inner diameter and length	2.26		
	0.00		
Wire diameter (dw)	4		
	0.69		
Porosity (γ)	7		

There is one row of 80 circumferential heater tubes on the engine. As shown in Fig. 3.1, these tubes are split into two sets and placed alternately with a slight clearance. A heater header, a horizontal annular manifold, connects these two sets of tubes. The tubes of one set come to an end at the regenerator intake. Gas from the regenerator travels up these tubes, through the common annular header, and into the tubes that point downward and are soldered into the hot cylinder's top.

Eight cartridges that are arranged circumferentially around the cylinder make up the regenerator. Each regenerator has a wire mesh screen matrix that is placed on top of one another. The matrix is made of the same material as the entire engine.

The cooler is made up of 312 circular tubes with a modest diameter that is arranged in a shell-and-tube pattern. The coolant for this cooler is water. 39 tubes are grouped in the

cooler thanks to an adaptation in design between the regenerator and cooler. Each cooler's end empties into a cooler end cap. Through a duct known as the cooler end connecting duct, this cap is joined to the cylinder. Stainless steel, which has a thermal conductivity of 15.5 W/m.K, is used throughout the engine.

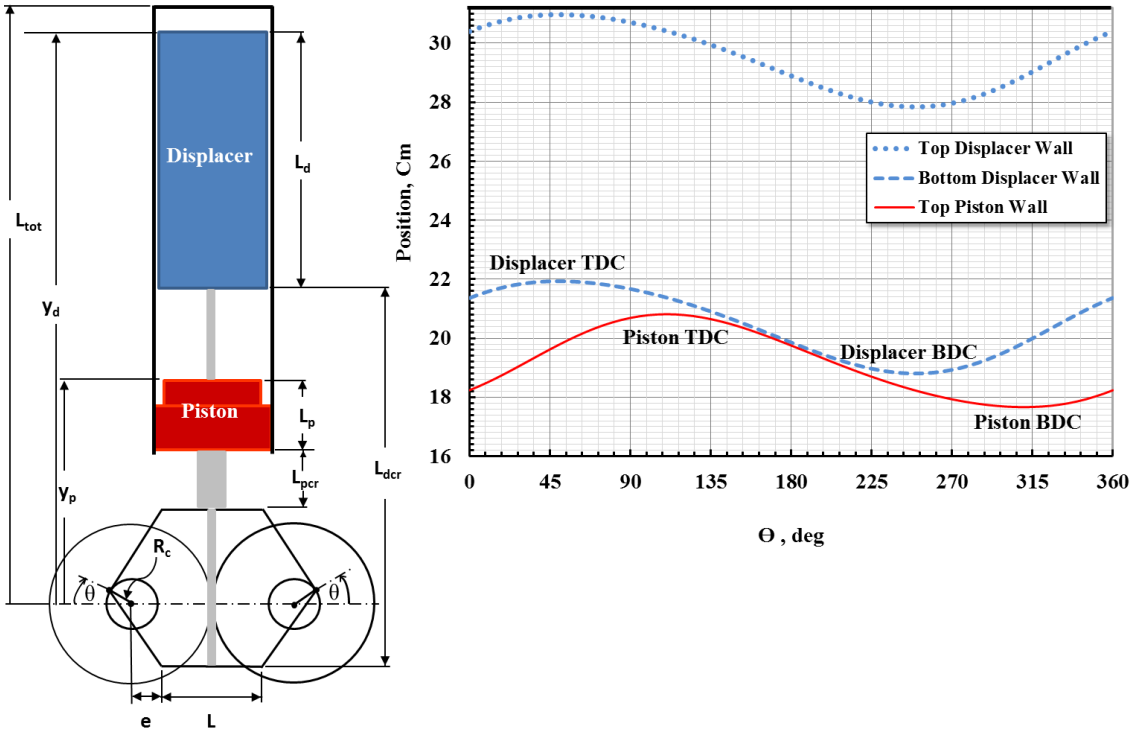

Figure 3.3 Kinematic analysis of the rhombic drive mechanism: piston and displacer displacement variations versus crank angle

Rhombic drive mechanism a unique mechanism for the β-type Stirling engine, is used here. The displacer and power piston rods are linked to two cranks that are geared together to counter-rotate and drive the yokes. The rhombic drive mechanism is a symmetrical mechanism that reduces the lateral force acting perpendicular to the axis by reducing the coaxial motion of the displacer and piston [78]. There are no sinusoidal volume changes due to this mechanism. As shown in Fig. 3.3, the kinematics of the drive mechanism and the geometrical characteristics of the cylinder are used to determine the precise functions of compression and expansion volumes.

The displacement of the piston and displacer, yp (θ) and yd (θ), as a function of the crank angle can be deduced from Fig. 3.3 as follows:

$$y_p(\theta) = R_C \sin\theta + \sqrt{[L^2 - (e + R_c \cos\theta)^2]} + L_{pcr} + L_p \qquad (3.1)$$

$$y_d(\theta) = R_C \sin\theta - \sqrt{[L^2 - (e + R_c \cos\theta)^2]} + L_{dcr} + L_d \qquad (3.2)$$

The instantaneous velocities of the piston and displacer, vp (θ) and vd (θ), are subsequently determined by differentiating Equations:

$$v_p(\theta) = \omega_r R_C \left\{\cos\theta + \frac{(e+R_c\cos\theta)\sin\theta}{\sqrt{[L^2-(e+R_c\cos\theta)^2]}}\right\} \quad (3.3)$$

$$v_d(\theta) = \omega_r R_C \left\{\cos\theta - \frac{(e+R_c\cos\theta)\sin\theta}{\sqrt{[L^2-(e+R_c\cos\theta)^2]}}\right\} \quad (3.4)$$

Then, the actual volume variations of compression and expansion spaces, Vc (θ) and Ve (θ), are functions of the engine's numerous geometric parameters and can be further defined as:

$$V_c(\theta) = \frac{\pi}{4} d_b^2 \left(y_d(\theta) - L_d - y_p(\theta)\right) \quad (3.5)$$

$$V_e(\theta) = \frac{\pi}{4} d_b^2 \left(L_t - y_d(\theta)\right) \quad (3.6)$$

where d_b is the mean bore of the cylinder.

Table 3.2 Baseline Operating condition of the GPU-3 Stirling engine

Working Fluid	Helium
Engine speed	3500 rpm
Mean pressure of compression space	4.14 MPa
Average gas temperature in heater	977 K
Metal-wall temperature of Cooler	293 K

3.2 Governing Equations

In this investigation, the flow is considered oscillatory, viscous, compressible, and Newtonian. The Unsteady Reynolds-Averaged Navier-Stokes (URANS) equations can be derived, in tensor form, by considering a cartesian coordinate system and decomposing the flow variables into ensemble-averaged values, u, T, and p, and fluctuations, $\acute{u}$, $\acute{T}$, and $\acute{p}$. Equation for conservation of mass:

$$\frac{\partial \rho}{\partial t} + \frac{\partial}{\partial x_i}\left(\rho u_{r_i}\right) = 0 \qquad (3.7)$$

3.2.1 Equations for conservation of momentum:

$$\frac{\partial(\rho.u_i)}{\partial t} + \frac{\partial\left(\rho.u_{r_j}.u_i\right)}{\partial x_j} = -\frac{\partial p}{\partial x_i} + \frac{\partial}{\partial x_j}\left[\mu.\left(\frac{\partial u_i}{\partial x_j} + \frac{\partial u_j}{\partial x_i}\right) + \lambda.\delta_{ij}.\frac{\partial u_k}{\partial x_k} - \rho.\overline{\acute{u}_i.\acute{u}_j}\right] \qquad (3.8)$$

where λ is the bulk viscosity coefficient; according to the Stokes hypothesis, it can be written as [85]:

$$\lambda = -\frac{2}{3}\mu$$

and δ_{ij} is Kronecker-Delta operator which either equals one if i = j or zero if i≠ j.

The Boussinesq approximation postulated that Reynolds stresses $\left(-\rho.\overline{\acute{u}_i.\acute{u}_j}\right)$ can be modelled with turbulent viscosity, t, which is similar to molecular viscosity. The approximation is therefore [87]:

$$-\rho.\overline{\acute{u}_i.\acute{u}_j} \approx \mu_t.\left[\left(\frac{\partial u_i}{\partial x_j} + \frac{\partial u_j}{\partial x_i}\right) - \frac{2}{3}.\delta_{ij}.\frac{\partial u_k}{\partial x_k}\right] - \frac{2}{3}.\rho.k.\delta_{ij} \qquad (3.9)$$

Where k is turbulent kinetic energy.

3.2.2 Equation for conservation of energy:

$$\frac{\partial(\rho.E)}{\partial t} + \frac{\partial}{\partial x_i}\left[u_{r_i}(\rho.E + p)\right] = \frac{\partial}{\partial x_i}\left[K_{eff}.\frac{\partial T}{\partial x_i} - \rho.C_p.\overline{u_i.\acute{T}}\right] + \varphi \qquad (3.10)$$

where φ is the viscous dissipation term while K_{eff} is the effective thermal conductivity, defined as:

$$K_{eff} = K + K_t \qquad (3.11)$$

where K and K_t is the laminar and turbulent thermal conductivity, respectively.

Equations of State

$$P.V = m.R.T \qquad (3.12)$$

3.2.3 Regenerator Equations

The regenerator is typically represented in the multi-dimensional analysis utilising the porous media approach [68], [69], [73]. Heat transfer and flow friction are the primary physical phenomena that need to be taken into account while characterising the regenerator [88].

Flow modeling in porous media

Adding a source term to the momentum equations in each of the three coordinate directions (x, y, and z) model the flow through the porous medium [85]:

$$S_i = -\left(\frac{\mu}{\alpha_r} u_i + C_2 \frac{1}{2} \rho u_i . |u_i|\right) \tag{3.12}$$

where $\frac{1}{\alpha_r}$ and C2 are the viscous and inertial resistance coefficients, respectively. These coefficients are hydrodynamic characteristics connected to the porous media's structure. The polynomial curve that modifies the data points showing the flow friction coefficient vs. Reynolds number through the regenerator can be used to derive these parameters in general. The friction coefficient, C_f, and Reynolds number are currently correlated using the conventional two parameter Ergun form [89], as shown :

$$C_f = \frac{a_1}{Re} + a_2 \tag{3.13}$$

According to this correlation, the coefficients can be written as:

$$\frac{1}{\alpha_r} = \frac{1}{2} a_1 \frac{1}{\gamma d_h^2} \tag{3.14}$$

$$C_2 = \frac{a_2}{\gamma^2 d_h} \tag{3.15}$$

where γ and d_h represent the matrix's porosity and hydraulic diameter, respectively. According to Walker and Vasishta [90], the hydraulic diameter is related to the wire diameter (d_w) as::

$$d_h = \frac{\gamma d_w}{(\gamma \mu_f)}$$

and Re is obtained by:

$$Re = \frac{\rho u d_h}{\gamma \mu_f}$$

where μ_f is the viscosity of the working fluid.

3.2.4 Heat Transfer modeling in porous media

In the present work, the local thermal non-equilibrium (LTNE) approach is chosen to model the heat flow within the regenerator. For solid matrix and fluid flow, a dual cell method is assumed [85]. Energy transfer between the two phases must be accounted for,

requiring the inclusion of additional inputs. This source term appears in the equations for fluid and matrix energy.

Equation for conservation of energy in Fluid zone:

$$\frac{\partial}{\partial t}\left(\gamma.\rho_f.E_f\right)+\frac{\partial}{\partial x_i}\left[u_i\left(\rho_f.E_f+p\right)\right]=\frac{\partial}{\partial x_i}\left[\gamma.K_f.\frac{\partial T_f}{\partial x_i}\right]+\varphi+h_{fs}.A_{fs}.\left(T_f-T_s\right) \quad (3.16)$$

Equation for conservation of energy for solid matrix:

$$\frac{\partial}{\partial t}\left[(1-\gamma).\rho_s.E_s\right]=\frac{\partial}{\partial x_i}\left[(1-\gamma).K_s.\frac{\partial T_f}{\partial x_i}\right]+h_{fs}.A_{fs}.\left(T_s-T_f\right) \quad (3.17)$$

where h_{fs} is the heat transfer coefficient at the interface between a fluid and a solid and A_{fs} is the interfacial area density. It should be noted that the thermal conductivity K_f of a fluid incorporates the turbulent contribution K_t.

Generally, the heat transfer coefficient is defined by:

$$h_{fs}=\frac{NuK_f}{d_h}$$

Nusselt number can be correlated with Reynolds number using a form of equation with two coefficients:

$$Nu=a_3Re+a_4 \quad (3.18)$$

where Nu is the Nusselt number.

The interfacial area density (Afs) can be derived as:

$$A_{fs}=\frac{4\gamma}{d_h}$$

3.2.5 Work and heat equations

Work per cycle is calculated by integrating the enclosed area of the p-V diagram for the compression and expansion spaces as follows:

$$W_{ind}=\oint p_e.dV_e+\oint p_c.dV_c \quad (3.19)$$

The work delivered to the power piston surface per cycle is calculated as:

$$W_{piston}=\oint\left(\int_{piston}p.dA\right).dy \quad (3.20)$$

Thus, the power can be expressed as the product of the work by the operating speed:

$$P = \left(\frac{\omega_r}{2\pi}\right).W$$

The cyclic heat transfer rate along any solid boundary can be computed from the integration:

$$Q = \left(\frac{\omega_r}{2\pi}\right)\oint\left(\int_{wall} q\, dA\right) dt \tag{3.21}$$

3.3 CFD Simulation

The commercial CFD software ANSYS FLUENT, v2022 R1, is used to implement the current simulation. Based on literature survey, Realizable k-ε turbulent model with enhanced wall treatment (EWT), was found to be most accurate [80] and is used to model the flow. The following subsections provide an explanation of the computational process and specifics of the CFD model used in this simulation.

Table 3.3 Operating conditions of GPU-3 Stirling Engine

Working Fluid	Air
Engine speed	2500 rpm
Mean pressure of compression space	4.14 MPa
Average gas temperature in heater	977 K
Metal-wall temperature of Cooler	293 K

3.3.1 Grid and Computational Domain

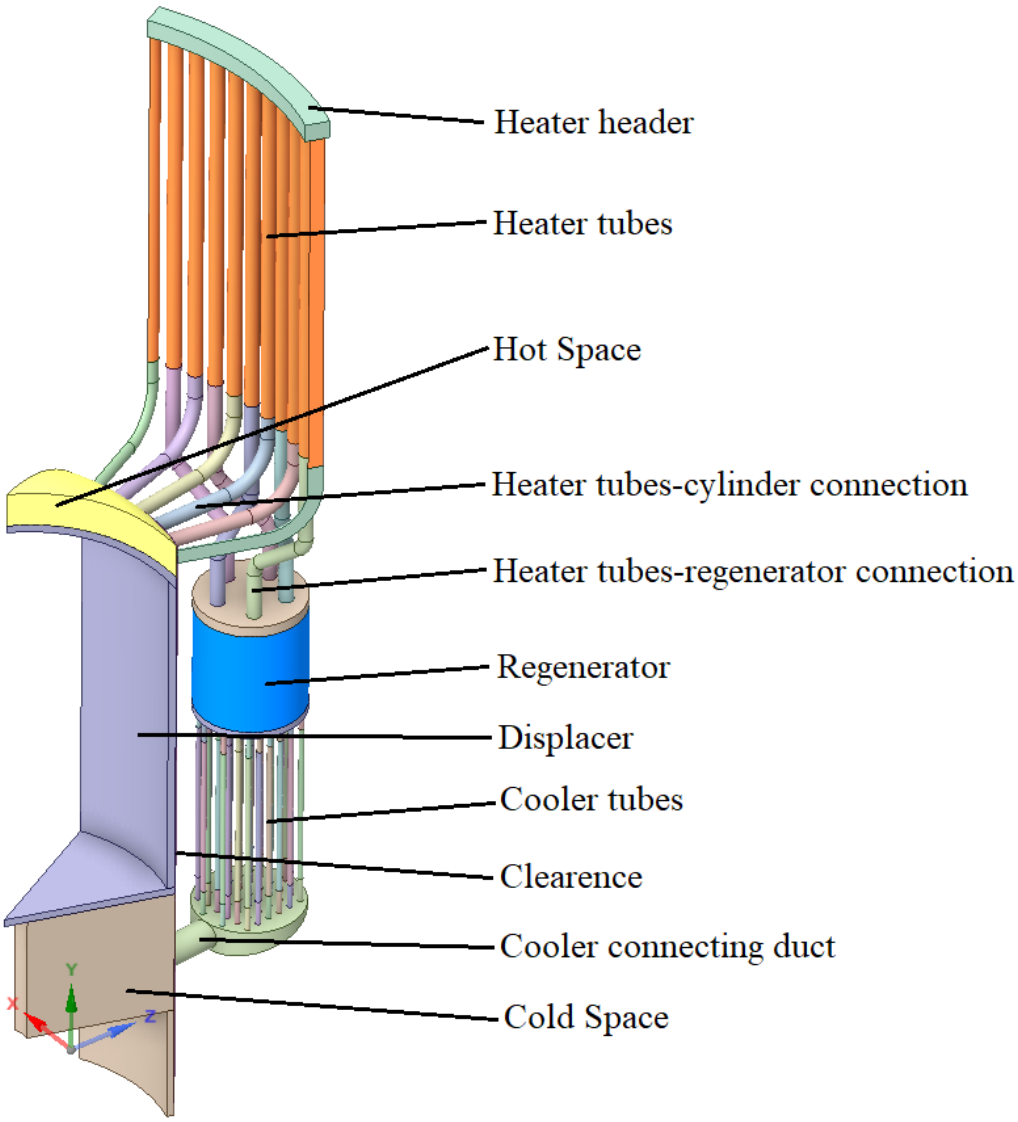

Figure 3.4 Computational domain of GPU3 Stirling Engine

As shown in Fig. 3.4, the engine geometry is precisely symmetrical about the cylinder axis. In this simulation, only one-eighth of the geometry is used as the computational domain to reduce the computational cost. The domain also contains the compression and expansion spaces, appendix gap, heater, regenerator, cooler, and cooler-end connecting duct, in addition to the displacer material. Except for the displacer, none of the component walls are considered.

Fig 3.5. shows the computational domain's configuration as expressed by the computational grid. The engine's initial configuration is shown in the figure when the crank angle is equal to 0º. Using SolidWorks v2020 and Mesh (Fluent), respectively, the

domain's CAD geometry and grid are produced. Due to its complex geometry, the computational domain is divided into 13 distinct sub-volumes with varying topologies. They are all meshing individually. Connecting the faces of adjacent volumes with arbitrary interfaces ensures the connectivity of the numerous subvolumes. Based on the character of each adjacent sub-volume, which may be deforming, rigid body motion, or static zones, a sliding or static interface is utilized [82].

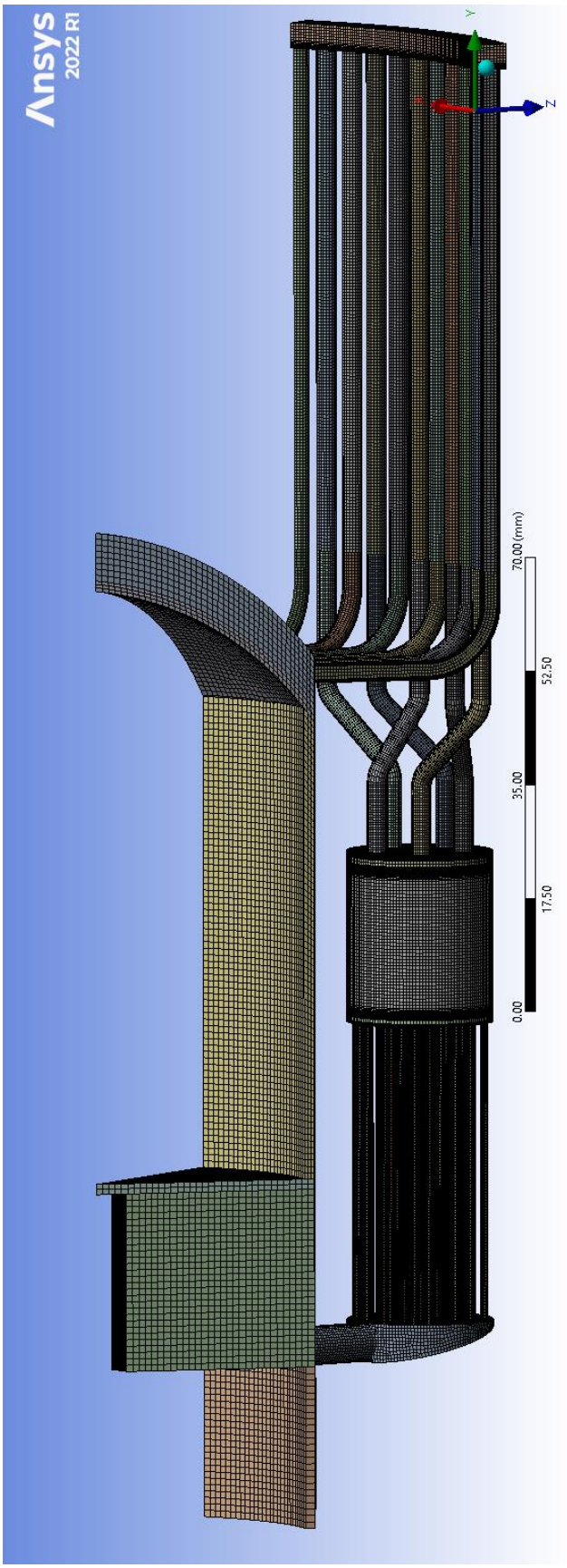

Figure 3.5 Mesh of Computational Domain

During the meshing phase, certain guidelines were followed to facilitate the application of transitional and low-Re turbulence models and to improve the accuracy and convergence of the solution. First, the grid is constructed primarily from hexahedral elements, with tetrahedral elements making up the remainder. Creating a lattice of hexahedral cells in complex geometries is significantly more difficult than with tetrahedral cells. Due to its ability to reduce the danger of numerical diffusion and the need for computational memory, it is more suitable for the current situation [71].

Second, places, where substantial gradients of flow variables are anticipated, are carefully refined, such as areas of area change, areas near wall boundaries, as well as areas surrounding abrupt curves and corners. In particular, as many cells as feasible with y+ 1 should cover the boundary layer in the normal direction. This is a suggestion for the creation of low-Re grids and precise heat transport phenomenon forecasting [91]. All engine walls—aside from those that move—undergo this refining. This is explained by the fact that moving borders necessitate an adaptive refining method, which significantly lengthens the computation time.

Thirdly, the mesh is accurately condensed on both sides at the fluid-solid interface to capture the conjugate heat transfer physics at the displacer walls. Two spatially contiguous grids are utilised in relation to the unique topology of the regenerator, which consists of two contiguous zones, one for the solid matrix and the other for the fluid. To precisely capture the impact of flow jets entering the regenerator, the grids at both extremities of the regenerator should be refined.

Lastly, there should be no abrupt changes in the size of the grid cells when moving from tiny to large items. In order to maintain the total number of elements as low as possible, areas of low interest may contain relatively large elements.

3.3.2 Boundary and Initial Conditions

Defining the boundary conditions that represent the actual case is a crucial step in CFD implementation. Since only one-eighth of the physical domain is being simulated, periodic azimuthal boundary conditions are applied to the faces in this sector. All stationary and moving walls have nonslip boundary conditions assigned.

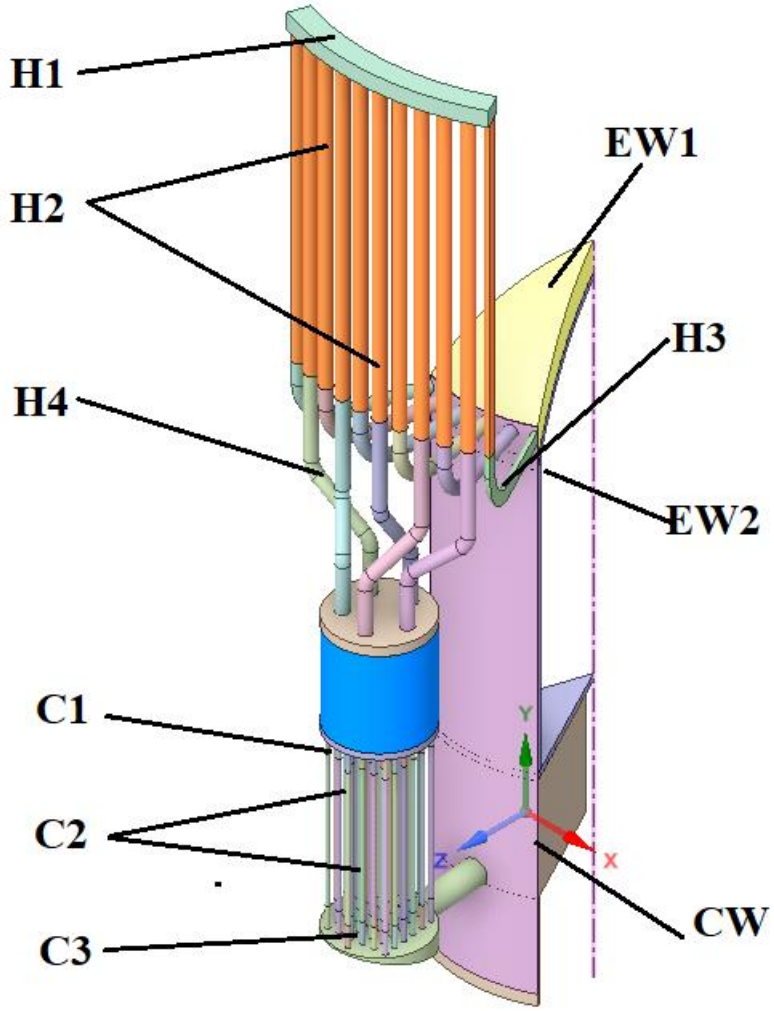

Figure 3.6 Walls names for computational domain

The displacer's interior walls are assumed to be adiabatic, while the piston's walls are assumed to be maintained at 305 K. As shown in Table 3.4, it is important to note that the operating condition does not specify the heater tube wall temperature explicitly. Therefore, this temperature was obtained through iteration in order to satisfy two criteria. The first objective is to produce an average cyclic gas temperature in the cylinders of approximately 977 Kelvin. Second, the heat supplied to the engine should be restricted to the length of the tubes exposed to the heat source, while the remainder of the tubes should maintain a virtually zero cyclic heat transfer rate.

Similarly, cooler wall temperatures are enforced. The solid material's higher thermal inertia than that of the gas enables the assumption of an isothermal wall boundary

temperature for expansion and compression spaces. The presumed wall temperature approximates the average temperature of each compartment's cyclic gas. Figure 3.4 and Table 3.4 depict the representation and values of the assumed temperatures of heater, cooler, expansion, and compression space walls utilised in the current simulation. The remaining components' walls exhibit a linear temperature distribution.

After multiple iterations, the initial pressure is chosen to be marginally higher than the cycle's minimal pressure. For this calculation, the cycle begins at $\theta = 0$ with an initial pressure of 3.8 MPa.

Table 3.4 Wall temperatures of GPU-3 Stirling Engine

Wall Name	Temperature (K)
EW1	870
EW2	805
H1	995
H2	1090
H3	1025
H4	975
C1	315
C2	293
C3	307
CW	325

3.3.3 Solution Scheme

Using the finite volume-based solver FLUENT, the governing equations are discretized and sequentially solved. A transient, pressure-based, segregated SIMPLEC solver with an absolute velocity formulation has been implemented for the simulation's

resolution. The thermophysical properties of the working gas (viscosity, specific heat, and thermal conductivity) are temperature dependent. The least squares method was used to compute the gradients of the transport quantities on the faces of the cell boundaries. Other spatial discretization techniques used in simulations are standard for the pressure term and second-order upwind for continuity, momentum, energy, and flow models' transport equations. For density, energy, and turbulence quantities, the under-relaxation factor of 0.9 is used. For discretizing the temporal derivatives, an implicit formulation of the first order is used. For all flow models, FLUENT 2022R1 is used with the default parameters.

As an approach to accelerating calculation convergence, the simulation is initialised with a steady-state solution that excludes piston and displacer motion but includes heat transfer calculations. Due to the movement of the power piston and displacer, the case becomes transient and grid deformation takes place. The standard k- turbulence model, the local thermal equilibrium porous media approach, and the absence of conjugate heat transfer are required to satisfy the convergence criteria during the first cycle of transient solution. During this cycle, low relaxation factor first-order upwind spatial discretization schemes are also employed. When the fundamental parameters are enabled and the first cycle reaches convergence, the calculation advances steadily toward convergence.

Using the dynamic mesh technique, the reciprocating motion of the piston and displacer and, consequently, the moving and deforming volumes are simulated. User Defined Functions (UDFs) are created and connected to FLUENT in order to control the motion of the piston and displacer; based on Equations (4.3, 4.4). Grid layering is used to prevent skew cells when the displacer is at the Top Dead Centre (TDC) in the expansion space [82] or when the compression space is completely compressed.

The porous media model requires the introduction of flow resistance and heat transfer coefficients empirically derived from Tew et al. [73] experimental findings. The GPU-3 regenerator's experimental data were presented as friction factor and Nusselt number as functions of Reynolds number. By fitting these data to Equations (4.17, 4.25) it is possible to determine the friction correlation constants, a1 and a2, as well as the Nusselt correlation constants, a3 and a4 [80].

On the basis of the proposed correlation, Eqs. (4.18, 4.19) are used to compute the simulation-constant values of the resistance coefficients, $1/\alpha$ and C_2. The fluid-to-matrix variable heat transfer coefficient is defined using a UDF and Equations (4.24, 4.25). Table

3.5 summarises the resistance coefficients, interfacial area density, and Nusselt correlations for the GPU-3 Stirling engine regenerator. The superficial velocity approach is used to simulate porous media because it is numerically more stable.

Table 3.5 Resistance coefficients, interfacial density and nusselt correlations for regenerator of GPU-3 Stirling Engine [80]

$1/\alpha$ $(1/m^2)$	$6.0183 \times 10^{+9}$
C_2 (1/m)	$1.2702 \times 10^{+4}$
A_{fs} (1/m)	30,304.4341
Nu	If Re<25 Nu=0.2022Re - 0.3534
	If Re>=25 Nu=0.0738Re + 2.9446

Due to the transient nature of the current case, the convergence of the simulation is determined by two primary criteria. The first is the residuals of the transport equations. The convergence criterion for each cycle is set to 1×10^{-6} for energy and 1×10^{-3} for all other equations. The second criterion for convergence is the monitoring of particular quantities to corroborate that the cyclic steady-state solution has been attained. The variation in average gas temperature across the thirteen subdomains is monitored for this purpose. In order to achieve the cyclic steady state, the deviation in these values over two cycles must be less than 1%. Each simulation requires approximately six cycles for the solution to become cyclic, with each cycle requiring approximately 36 hours on a Core i7-12700 processor with a clock speed of 2.1 GHz and 16 GB of dynamic memory.

3.4 Model Validation

In order to validate the computational results, a comparison is made between the present simulation's estimated indicated power and thermal efficiency and the experimental results of the GPU-3 engine, which are summarised in [18, 19]. The default operational condition is illustrated in the diagram. In this instance, the realisable k-turbulence model with improved wall treatment is utilised.

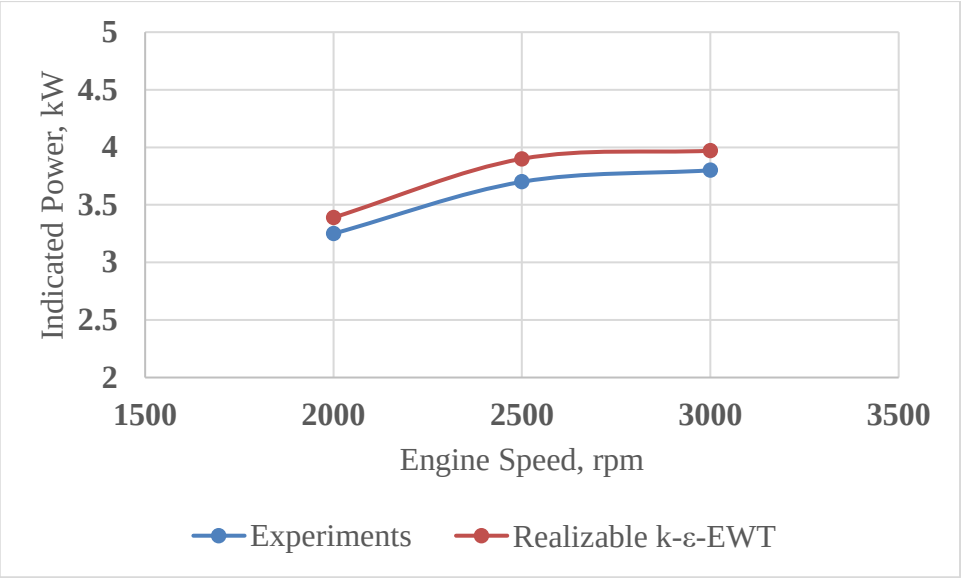

Figure 3.7 Predicted Indicated Power Vs Experimental Values for Helium

The comparison suggests that the current CFD simulation corresponds closely to the experimental outcome. The simulation overestimated power and efficiency by approximately 11% and 6%, respectively. Interestingly, the variance of predicted power is greater than that of predicted efficiency.

In this instance, CFD modelling appears to be more accurate. The present results have inaccuracies due to the unaccounted-for effects of flow leakage from the cylinder to the buffer space through the piston rings and heat conduction loss through the material thickness.

CHAPTER 4 RESULTS AND DISCUSSION

4.1 Flow characteristics

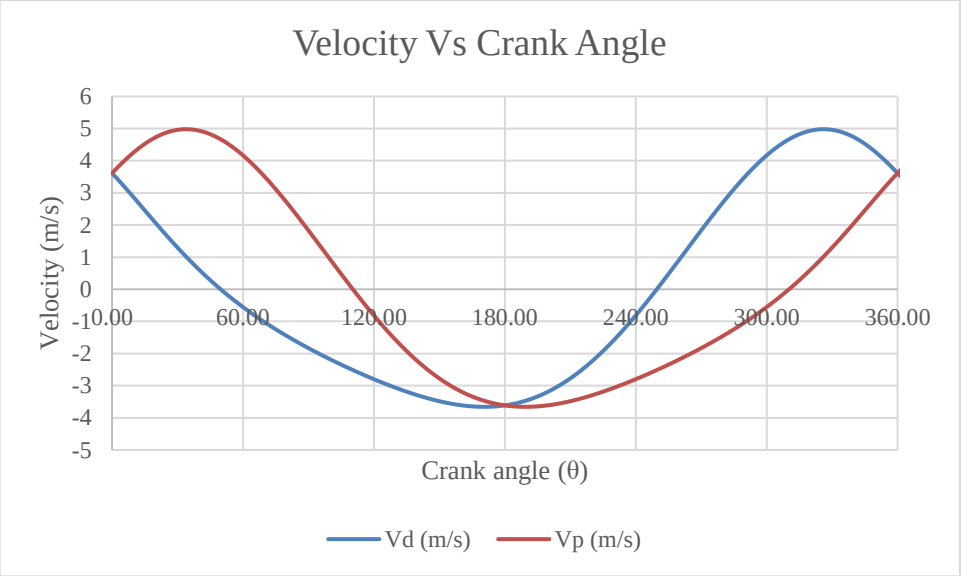

Figure 4.1 Velocity of Displacer piston and Power piston as a fuction of crank angle

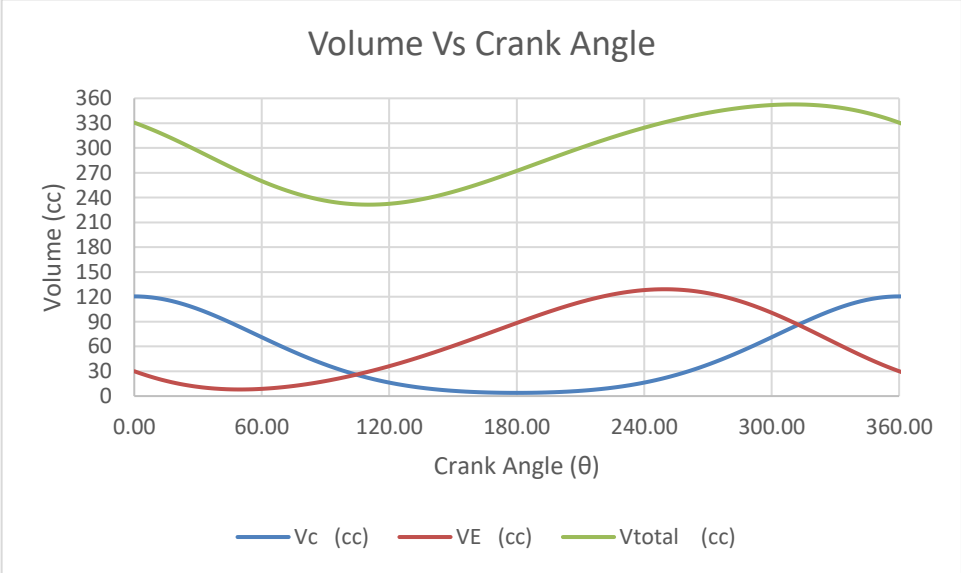

Figure 4.2 Volume variation in compression space, expansion space and total space as a function of crank angle

During a complete cycle, depicted in Fig. 4.2, the instantaneous fluctuations of the total, expansion space, and compression space volumes as a function of the crank angle.

Working volume and inactive volume are included in the total volume. Maximum and minimum total engine volumes occur at the Bottom Dead Centre (BDC) and Top Dead Centre (TDC) of the power piston, which results in 1.519 compression ratio. In addition, 62% of this engine's total volume is comprised of average inactive volume.

The sum of the pressure drops in the heater, regenerator, cooler, and manifolds relative to the flow direction equals the pressure differential between the compression and expansion spaces. The difference between the compression space's pressure and the pressure on the piston wall is the result of the pressure loss brought on by the finite speed of the piston [71]. The pressure waves produced by the movement of the piston are what cause the difference between the gas pressure above the moving piston and the mass gas pressure inside the cylinder, according to the direction of the flow. As a result, Equation (31), which calculates the work provided to the power piston, calculates less work than Equation (30), which calculates the work indicated.

Notably, the error in power prediction is primarily attributable to inaccurate predictions of the pressure phase angle, i.e. the angle between TDC and the maximal gas pressure [92].

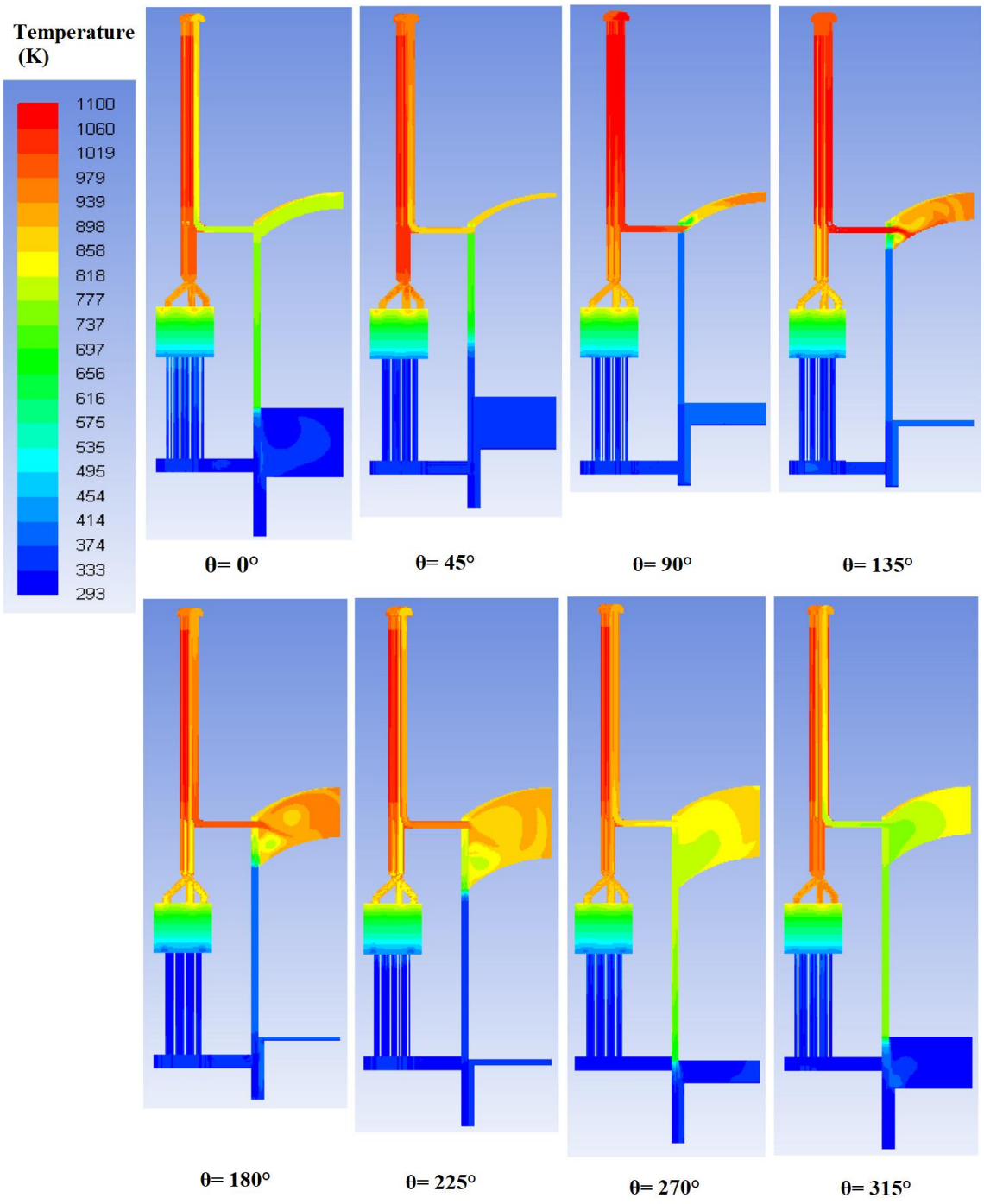

Figure 4.3 Variations of average gas temperature within the compression space, expansion space, heater, chiller, and regenerator as a function of crank angle

Each volume's temperature variation seems to diverge greatly from the harmonic distribution. This outcome deviates from that which was predicted by the GPU-3 engine's second- and third-order models, which showed that the temperature distribution was quite similar to a sinusoidal profile [23], [93], [94]. This is because these models are unable to accurately depict the intricate interactions between fluid dynamics and heat transfer phenomena that take place inside the engine. The temperature contours of the whole flow

domain are shown in Figure 4.3 for eight different crank angles throughout the course of a full cycle.

As shown in Figure 4.2, the power piston and displacement are nearly at their BDC and TDC at the beginning of the cycle, when the volume of the compression space is at its maximum. The compression and expansion spaces are compressed concurrently as they ascend. Now, the gas moves through the appendix gap and three heat exchangers as it moves from the expansion space to the compression space. A comparatively hot thermal plume appears in the compression region as a result of the mixing of the hot gas jet from the appendix gap with the less hot gas jet from the cold-end connection, as shown in Figure 4.3.

The displacer's velocity reduces as it moves steadily towards its TDC, which happened at an angle of 51,4°, leading to a progressive change in the flow direction from the compression region to the expansion space. Gas is moving through the two channels from the compression space to the expansion space as the displacer is close to its TDC at an angle of $\theta = 45°$. However, a tiny amount of hot gas still leaks from the expansion space through the heater pipes, which the displacer has only partially stopped. The flow direction via the heater tubes reverses at this particular instant. The displacer facilitates expansion of the expansion space after attaining TDC and moving downward. The amount of cold flow from the compression space through the appendix gap into the expansion space also rises as the displacer is driven downward. This phenomenon explains why the average gas temperature of the expansion space abruptly dropped at the start of the expansion stroke, as shown in Figure 4.3 at roughly a 90-degree crank angle. The compression space is at its greatest compression when the piston reaches TDC and starts to reverse direction. As a result, this area releases large amounts of flow in the direction of expanding space. This also explains why the heater's gas temperatures were higher than usual at this time. As a result, the cycle pressure keeps increasing even while the engine's overall volume increases. The flow field is dominated by a pair of counter-rotating vortices with different intensities during the expansion stroke of the expansion space. When the piston velocity is at its highest, between 180° and 225°, this flow characteristic is more obvious. As seen in Figure 4.4, even though these vortices enhance the space's mixture, the average gas temperature of this area nevertheless drops dramatically as a result of the expansion stroke's constant motion. The flow progressively changes course a second time when the displacer gets closer to its BDC, switching from

the expansion space to the compression space. Figure 4.3 show how the appendix gap and heat exchangers introduce gas into the compression space during the expansion stroke. As seen in Figure 8, the gas temperature in the compression region is essentially constant during this time. The two opposing effects—heating from the two gas jets entering the heated region and cooling from the volume expansion—lead to this.

4.1.1 Working spaces

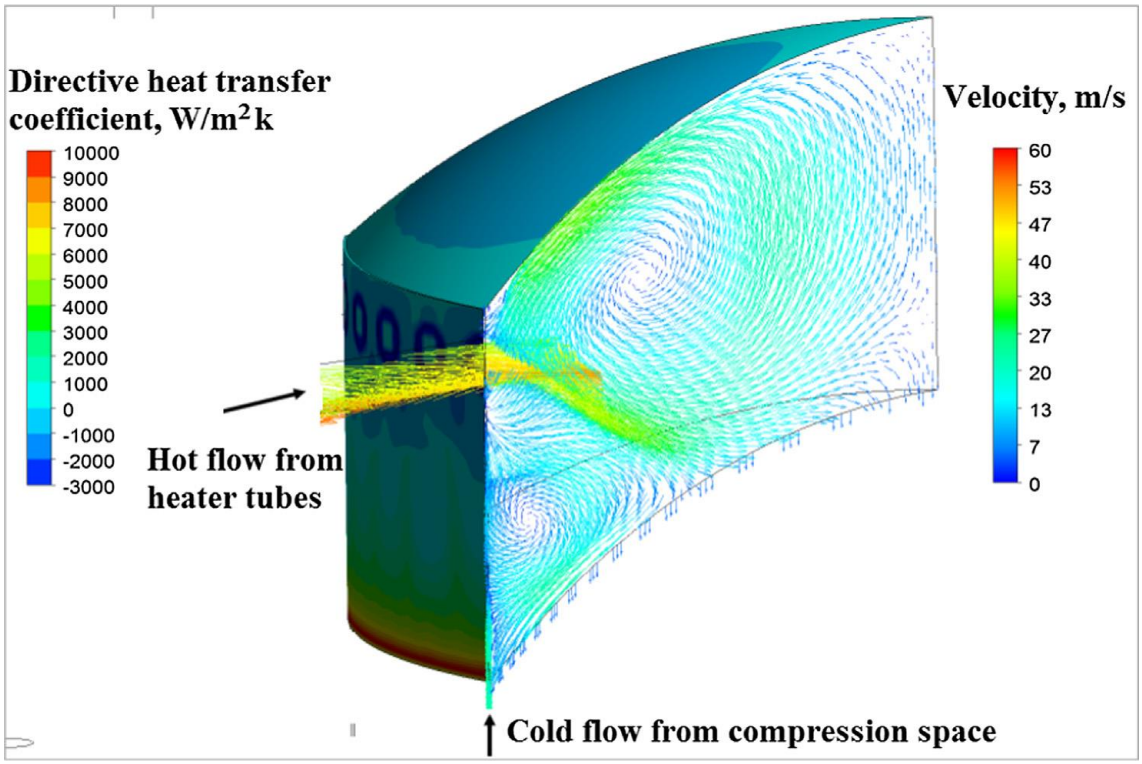

Figure 4.4 Velocity vector rendering in expansion space

Figure 4.2 shows, at a 180-degree angle, how the fluid flow field affects the local directed heat transfer coefficient on the expansion space walls. With the inclusion of a direction indicator, the directive heat transfer coefficient has the same value as the convective heat transfer coefficient in this instance. While the negative sign denotes heat transfer in the opposite direction, the positive sign shows heat transmission from the walls into the fluid zone. It is very interesting to see the huge range of coefficient variations on each wall. This finding supports and agrees with assertion by Chen et al. [68] that the constant heat transfer coefficient premise is flawed.

As previously indicated, two tumbles, or counter-rotating vortices, frequently emerge together with the flow coming from the heater and appendix gap inside the expansion space. In reciprocating engines, the term "tumble vortex" is frequently used to describe a

rotational motion about the circumferential axis of a cylinder. This 3D phenomena and its effects are vividly shown in Figure 4.4. The hot jet entering from the heater pipes heats the upper wall of the cylinder due to the impingement heat transfer caused by the dominant tumbling vortex. The cylinder's lateral wall is concurrently subject to two different effects. The appendix gap jet produces the cold flow of the corner tumble vortex, which quickly cools the object. Due to the dominance of the heating effect of the vortex, this effect gradually decreases upward. The heat transfer coefficient shifts from highly positive values in the area where the corner vortex impinges to comparatively high negative values in the area where the dominating vortex impinges as a result of these contradicting effects.

The heat transfer rates at the expansion space's top and side walls display nearly comparable trends early in the cycle. However, substantial differences start to show up following the jetting of flow entering from the compression area, between around 51.4° and 250° of crank angle. This is because each wall is being affected differently by the tumble vortex, as was previously mentioned. Heat transfer rates considerably decrease during the compression stroke of the expansion region, which is accompanied by the ejection of flow from it. It results from tumbling vortices dissipating and their resulting impacts. The findings of Chen et al. [68], who noticed that the ejection process enhances heat transfer in a way similar to that of impingement, are in conflict with this result.

The impact of the fluid flow field on the convective heat transfer processes within the compression space can also be explained. Figure 4.4 shows this effect as well using the directed heat transfer coefficient. Similar impingement phenomena can be seen in the compression area, but only one tumble vortex is produced by the two hot jets coming from the expansion space. The side walls of the room rapidly warm up as a result of this vortex. The side wall and piston wall both indirectly benefit from the vortex's presence. By creating an entrainment effect, this vortex pulls the bulk flow of the area in its direction, creating a secondary vortex that spins in the opposite direction. Through the movement of cooler fluid close by, this vortex cools the side wall's bottom. Additionally, by steering heated fluid away from the piston wall, it lessens the rate of heat transfer. The piston, on the other hand, is not immediately exposed to impingement heat transfer because it is in motion. The gas flow within the compression region is rather warm due to the piston's upward motion, which heats it. The gas cools after changing directions,

which causes heat to move in the other way. There are various aberrations in the fluctuation of the piston's heat transfer rate when it reverses direction.

During the expansion impulses, the compression and expansion spaces' principal heat transfer rates happen. This is a result of the tumble vortices produced by the flow jetting within the voids having a considerable impinging effect.

4.2 Power

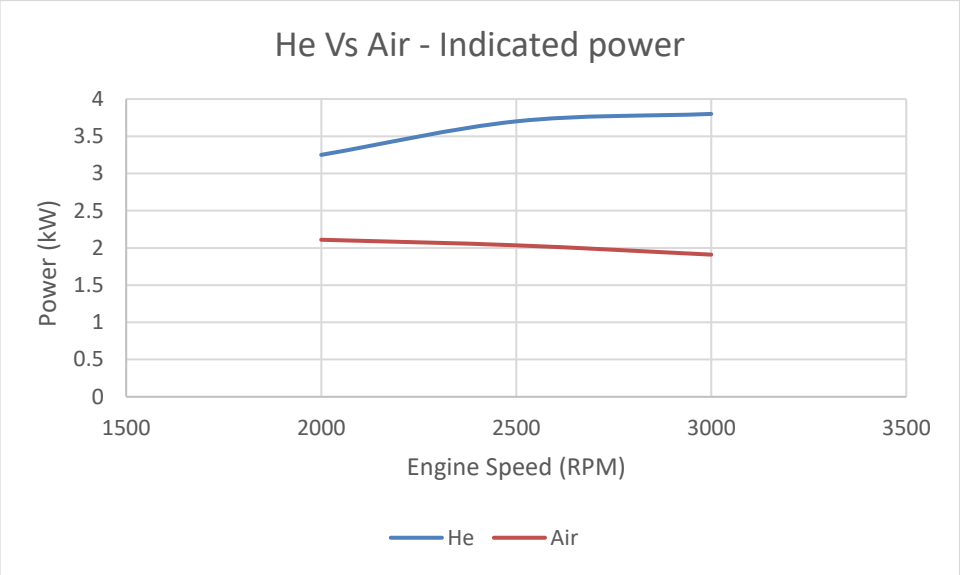

Figure 4.5 Comparison of Indicated Power Helium Vs Air

The power produced by air is low as compared to helium, owing to:-

- Molecular Weight: Helium has a much lower molecular weight than air. This means that helium molecules are lighter and can move more quickly, resulting in higher heat transfer rates.
- Specific Heat Capacity: Air has a higher specific heat capacity than air. Due to its lower specific heat capacity, helium can absorb and release heat more rapidly, leading to more efficient energy conversion in the Stirling engine.
- Thermal Conductivity: Air has a lower thermal conductivity compared to helium. With higher thermal conductivity, helium can transfer heat more effectively, resulting in better thermal efficiency and higher power output.

CHAPTER 5 CONCLUSION

Substantial progress has been made in recent years to improve the performance and application of solar-powered Stirling engines. CFD analysis is becoming the preferred choice for detailed performance evaluation of Stirling Engines.

- Hybrid systems, which include Dual Receivers, one for heating Oil and the other for producing electricity, are better at meeting the Heat & Power loads of a building. While the system, which includes seasonal geothermal storage, improves sustainability by utilising more renewable sources. But hybrid systems in which many subsystems are involved might improve overall efficiency but may increase complexity and drive up the setup and maintenance costs.
- The systems with Solar Stirling Engine mechanical output directly coupled with Pumps are simple, more efficient and thus better for field use as an Agricultural pump & Reverse Osmosis pump, unlike the systems that utilise electric pumps.
- The Hybrid Water Desalination system, which includes a Thermoelectric cooler and utilises the waste heat of a Solar Stirling Engine, is better than a conventional Solar Desalination system in terms of yield but is complex and costlier.
- CFD approach is the only approach capable of modelling conjugated flow and heat transfer processes while taking real geometries into account.
- The flow inside of almost all engine parts is spatially strongly non-uniform, and pressure and temperature distribution is inhomogeneous. Therefore, Full domain 3D CFD study is preferred over partial domain 3D and 2D CFD studies.
- The accuracy of the CFD study is improved by 11% by considering internal radiation heat transfer.

- ANSYS Fluent is the most popular choice among researchers for CFD analysis of the Stirling Engine.
- ANSYS Fluent is limited regarding the simultaneous use of the Porous media Local Non-Equilibrium Model (LTNE) with the Radiation model. Standard radiation models like Discrete Ordinates and Surface to Surface cannot be used with LTNE whereas models like Discrete Transfer Radiation Model and Monte Carlo Ray Tracing Method can be used with LTNE.
- Impinging effect is noticed in beta-type and gamma-type Stirling engines which leads to the formation of vortices and enhances heat transfer. These vortices can be predicted only by CFD analysis.
- There is a reduction in power output of the engine of about 40% with air as working fluid, compared to Helium.
- Power output of engine decreases with an increase in engine speed, indicating that air reduces the optimal engine speed as compared to helium.

REFERENCES

[1] J. A. Frankel, “The Natural Resource Curse: A Survey,” Mar. 2010, doi: 10.3386/W15836.

[2] M. Höök and X. Tang, “Depletion of fossil fuels and anthropogenic climate change—A review,” *Energy Policy*, vol. 52, pp. 797–809, Jan. 2013, doi: 10.1016/J.ENPOL.2012.10.046.

[3] R. B. Hiremath, B. Kumar, P. Balachandra, N. H. Ravindranath, and B. N. Raghunandan, “Decentralised renewable energy: Scope, relevance and applications in the Indian context,” *Energy for Sustainable Development*, vol. 13, no. 1, 2009, doi: 10.1016/j.esd.2008.12.001.

[4] B. Bhandari, K. T. Lee, C. S. Lee, C. K. Song, R. K. Maskey, and S. H. Ahn, “A novel off-grid hybrid power system comprised of solar photovoltaic, wind, and hydro energy sources,” *Appl Energy*, vol. 133, pp. 236–242, Nov. 2014, doi: 10.1016/J.APENERGY.2014.07.033.

[5] S. P. P. Sukhatme, J. K. Nayak, and J. K. Naik, *Solar Energy Principles of Thermal Collection and Storage*. 2014.

[6] G. Walker, “The Stirling engine,” *Sci Am*, vol. 229, no. 2, 1973, doi: 10.1038/scientificamerican0873-80.

[7] U. R. Singh and A. Kumar, “Review on solar Stirling engine: Development and performance,” *Thermal Science and Engineering Progress*, vol. 8, pp. 244–256, Dec. 2018, doi: 10.1016/j.tsep.2018.08.016.

[8] O. R. Sandoval, B. C. Caetano, M. U. Borges, J. J. García, and R. M. Valle, “Modelling, simulation and thermal analysis of a solar dish/Stirling system: A case study in Natal, Brazil,” *Energy Convers Manag*, vol. 181, pp. 189–201, Feb. 2019, doi: 10.1016/J.ENCONMAN.2018.12.005.

[9] M. E. Zayed, J. Zhao, A. H. Elsheikh, W. Li, and M. A. Elaziz, “Optimal design parameters and performance optimization of thermodynamically balanced dish/Stirling concentrated solar power system using multi-objective particle swarm optimization,” *Appl Therm Eng*, vol. 178, 2020, doi: 10.1016/j.applthermaleng.2020.115539.

[10] M. E. Zayed, J. Zhao, A. H. Elsheikh, W. Li, S. Sadek, and M. M. Aboelmaaref, “A comprehensive review on Dish/Stirling concentrated solar power systems: Design, optical and geometrical analyses, thermal performance assessment, and applications,” *Journal of Cleaner Production*, vol. 283. 2021. doi: 10.1016/j.jclepro.2020.124664.

[11] K. Bataineh, “Performance evaluation of a stand-alone solar dish Stirling system for off–grid electrification,” *Energy Sources, Part A: Recovery, Utilization, and Environmental Effects*, vol. 44, no. 1, pp. 1208–1226, Mar. 2022, doi: 10.1080/15567036.2022.2053249.

[12] S. Guarino, A. Buscemi, A. Messineo, and V. Lo Brano, “Energy and Environmental Assessment of a Hybrid Dish-Stirling Concentrating Solar Power Plant,” *Sustainability*, vol. 14, no. 10, p. 6098, May 2022, doi: 10.3390/su14106098.

[13] B. Shboul *et al.*, “Design and Techno-economic assessment of a new hybrid system of a solar dish Stirling engine instegrated with a horizontal axis wind turbine for microgrid power generation,” *Energy Convers Manag*, vol. 245, p. 114587, Oct. 2021, doi: 10.1016/j.enconman.2021.114587.

[14] E. A. Bekele and V. R. Ancha, “Transient performance prediction of solar dish concentrator integrated with stirling and TEG for small scale irrigation system: A case of Ethiopia,” *Heliyon*, vol. 8, no. 9, p. e10629, Sep. 2022, doi: 10.1016/j.heliyon.2022.e10629.
[15] D. Geng, J. Cui, and L. Fan, “Performance investigation of a reverse osmosis desalination system powered by solar dish-Stirling engine,” *Energy Reports*, vol. 7, pp. 3844–3856, Nov. 2021, doi: 10.1016/j.egyr.2021.06.072.
[16] G. Walker, *Stirling engines*. Oxford University Press,New York, NY, 1980.
[17] G. Walker, “ELEMENTARY DESIGN GUIDELINES FOR STIRLING ENGINES.,” *Proceedings of the Intersociety Energy Conversion Engineering Conference*, vol. 1, 1979.
[18] R. Ben-Mansour, A. Abuelyamen, and E. M. A. Mokheimer, “CFD analysis of radiation impact on Stirling engine performance,” *Energy Convers Manag*, vol. 152, pp. 354–365, Nov. 2017, doi: 10.1016/j.enconman.2017.09.056.
[19] M. Babaelahi and H. Sayyaadi, “A new thermal model based on polytropic numerical simulation of Stirling engines,” *Appl Energy*, vol. 141, pp. 143–159, Mar. 2015, doi: 10.1016/J.APENERGY.2014.12.033.
[20] K. M. Bataineh and M. F. Maqableh, “A new numerical thermodynamic model for a beta-type Stirling engine with a rhombic drive,” *Thermal Science and Engineering Progress*, vol. 28, p. 101071, Feb. 2022, doi: 10.1016/J.TSEP.2021.101071.
[21] E. Rogdakis, P. Bitsikas, G. Dogkas, and G. Antonakos, “Three-dimensional CFD study of a β-type Stirling Engine,” *Thermal Science and Engineering Progress*, vol. 11, pp. 302–316, Jun. 2019, doi: 10.1016/j.tsep.2019.04.012.
[22] I. Urieli, C. J. Rallis, D. M. Berchowitz, I. Urieli, C. J. Rallis, and D. M. Berchowitz, “Computer simulation of Stirling cycle machines,” *iece*, vol. 2, pp. 1512–1521, 1977, Accessed: May 16, 2023. [Online]. Available: https://ui.adsabs.harvard.edu/abs/1977iece.conf.1512U/abstract
[23] I. Urieli and D. Berchowitz, “Stirling cycle engine analysis,” 1984, Accessed: May 16, 2023. [Online]. Available: https://www.osti.gov/etdeweb/biblio/6068495
[24] Y. Li, S. S. Choi, and D. M. Vilathgamuwa, “Primary Frequency Control Scheme for a Fixed-Speed Dish-Stirling Solar-Thermal Power Plant,” *IEEE Transactions on Power Systems*, vol. 33, no. 2, 2018, doi: 10.1109/TPWRS.2017.2724557.
[25] L. S. Mendoza Castellanos *et al.*, “Experimental analysis and numerical validation of the solar Dish/Stirling system connected to the electric grid,” *Renew Energy*, vol. 135, 2019, doi: 10.1016/j.renene.2018.11.095.
[26] A. A. Lashari, P. H. Shaikh, Z. H. Leghari, M. I. Soomro, Z. A. Memon, and M. A. Uqaili, “The performance prediction and techno-economic analyses of a stand-alone parabolic solar dish/stirling system, for Jamshoro, Pakistan,” *Clean Eng Technol*, vol. 2, 2021, doi: 10.1016/j.clet.2021.100064.
[27] M. Vahidi Bidhendi and Y. Abbassi, “Exploring dynamic operation of a solar dish-stirling engine: Validation and implementation of a novel TRNSYS type,” *Sustainable Energy Technologies and Assessments*, vol. 40, 2020, doi: 10.1016/j.seta.2020.100765.
[28] K. Bataineh and Y. Taamneh, “Performance analysis of stand-alone solar dish Stirling system for electricity generation,” *International Journal of Heat and Technology*, vol. 35, no. 3, pp. 498–508, Sep. 2017, doi: 10.18280/ijht.350306.
[29] Y. Kadri and H. Hadj Abdallah, “Performance evaluation of a stand-alone solar dish Stirling system for power generation suitable for off-grid rural electrification,”

Energy Conversion and Management, vol. 129. 2016. doi: 10.1016/j.enconman.2016.10.024.

[30] E. K. Ezeanya, G. H. Massiha, W. E. Simon, J. R. Raush, and T. L. Chambers, "System advisor model (SAM) simulation modelling of a concentrating solar thermal power plant with comparison to actual performance data," *Cogent Eng*, vol. 5, no. 1, 2018, doi: 10.1080/23311916.2018.1524051.

[31] A. A. Lashari, P. H. Shaikh, Z. H. Leghari, M. I. Soomro, Z. A. Memon, and M. A. Uqaili, "The performance prediction and techno-economic analyses of a stand-alone parabolic solar dish/stirling system, for Jamshoro, Pakistan," *Clean Eng Technol*, vol. 2, 2021, doi: 10.1016/j.clet.2021.100064.

[32] M. Vahidi Bidhendi and Y. Abbassi, "Exploring dynamic operation of a solar dish-stirling engine: Validation and implementation of a novel TRNSYS type," *Sustainable Energy Technologies and Assessments*, vol. 40, 2020, doi: 10.1016/j.seta.2020.100765.

[33] M. E. Zayed, J. Zhao, A. H. Elsheikh, W. Li, and M. A. Elaziz, "Optimal design parameters and performance optimization of thermodynamically balanced dish/Stirling concentrated solar power system using multi-objective particle swarm optimization," *Appl Therm Eng*, vol. 178, 2020, doi: 10.1016/j.applthermaleng.2020.115539.

[34] K. Bataineh and Y. Taamneh, "Performance analysis of stand-alone solar dish Stirling system for electricity generation," *International Journal of Heat and Technology*, vol. 35, no. 3, pp. 498–508, Sep. 2017, doi: 10.18280/ijht.350306.

[35] L. Gu *et al.*, "Research on a new type of solar dish Stirling cogeneration system based on adjustable receiver and control strategy," *Energy Convers Manag*, vol. 249, 2021, doi: 10.1016/j.enconman.2021.114836.

[36] A. Bianchini, A. Guzzini, M. Pellegrini, and C. Saccani, "Performance assessment of a solar parabolic dish for domestic use based on experimental measurements," *Renew Energy*, vol. 133, 2019, doi: 10.1016/j.renene.2018.10.046.

[37] D. Papurello, D. Bertino, and M. Santarelli, "CFD performance analysis of a dish-stirling system for microgeneration," *Processes*, vol. 9, no. 7, 2021, doi: 10.3390/pr9071142.

[38] E. Açıkkalp, S. Y. Kandemir, and M. H. Ahmadi, "Solar driven Stirling engine - chemical heat pump - absorption refrigerator hybrid system as environmental friendly energy system," *J Environ Manage*, vol. 232, 2019, doi: 10.1016/j.jenvman.2018.11.055.

[39] F. Jabari, M. Nazari-heris, B. Mohammadi-ivatloo, S. Asadi, and M. Abapour, "A solar dish Stirling engine combined humidification-dehumidification desalination cycle for cleaner production of cool, pure water, and power in hot and humid regions," *Sustainable Energy Technologies and Assessments*, vol. 37, 2020, doi: 10.1016/j.seta.2020.100642.

[40] N. Merabet, L. Chouichi, and K. Kerboua, "Numerical design and simulation of a thermodynamic solar solution for a pilot residential building at the edge of the sun-belt region," *Environ Dev Sustain*, 2021, doi: 10.1007/s10668-021-01956-2.

[41] H. Allouhi, A. Allouhi, K. M. Almohammadi, A. Hamrani, and A. Jamil, "Hybrid renewable energy system for sustainable residential buildings based on Solar Dish Stirling and wind Turbine with hydrogen production," *Energy Convers Manag*, vol. 270, p. 116261, Oct. 2022, doi: 10.1016/J.ENCONMAN.2022.116261.

[42] I. Al Keyyam, M. Al-Nimr, S. Khashan, and A. Keewan, "A new solar atmospheric water harvesting integrated system using CPV/T – Stirling engine – Absorption

cooling cycle and vapor compression refrigeration cycle," *Int J Energy Res*, vol. 45, no. 11, pp. 16400–16417, Sep. 2021, doi: 10.1002/er.6888.

[43] L. Gu *et al.*, "Research on a new type of solar dish Stirling cogeneration system based on adjustable receiver and control strategy," *Energy Convers Manag*, vol. 249, 2021, doi: 10.1016/j.enconman.2021.114836.

[44] D. Papurello, D. Bertino, and M. Santarelli, "CFD performance analysis of a dish-stirling system for microgeneration," *Processes*, vol. 9, no. 7, 2021, doi: 10.3390/pr9071142.

[45] N. Merabet, L. Chouichi, and K. Kerboua, "Numerical design and simulation of a thermodynamic solar solution for a pilot residential building at the edge of the sun-belt region," *Environ Dev Sustain*, 2021, doi: 10.1007/s10668-021-01956-2.

[46] H. Allouhi, A. Allouhi, K. M. Almohammadi, A. Hamrani, and A. Jamil, "Hybrid renewable energy system for sustainable residential buildings based on Solar Dish Stirling and wind Turbine with hydrogen production," *Energy Convers Manag*, vol. 270, p. 116261, Oct. 2022, doi: 10.1016/J.ENCONMAN.2022.116261.

[47] S. Guarino, A. Buscemi, A. Messineo, and V. Lo Brano, "Energy and Environmental Assessment of a Hybrid Dish-Stirling Concentrating Solar Power Plant," *Sustainability*, vol. 14, no. 10, p. 6098, May 2022, doi: 10.3390/su14106098.

[48] I. Al Keyyam, M. Al-Nimr, S. Khashan, and A. Keewan, "A new solar atmospheric water harvesting integrated system using CPV/T – Stirling engine – Absorption cooling cycle and vapor compression refrigeration cycle," *Int J Energy Res*, vol. 45, no. 11, pp. 16400–16417, Sep. 2021, doi: 10.1002/er.6888.

[49] C. E. Andraka, "Dish Stirling advanced latent storage feasibility," in *Energy Procedia*, 2014. doi: 10.1016/j.egypro.2014.03.074.

[50] A. Mohammadnia, B. M. Ziapour, F. Sedaghati, L. Rosendahl, and A. Rezania, "Utilizing thermoelectric generator as cavity temperature controller for temperature management in dish-Stirling engine," *Appl Therm Eng*, vol. 165, 2020, doi: 10.1016/j.applthermaleng.2019.114568.

[51] F. Jabari, M. Nazari-Heris, B. Mohammadi-Ivatloo, S. Asadi, and M. Abapour, "Toward energy-efficient microgrids under summer peak electrical demand integrating solar dish Stirling heat engine and diesel unit," *Journal of Energy Management and Technology*, vol. 4, no. 3, 2020.

[52] M. Mehrpooya, N. Ghadimi, M. Marefati, and S. A. Ghorbanian, "Numerical investigation of a new combined energy system includes parabolic dish solar collector, Stirling engine and thermoelectric device," *Int J Energy Res*, vol. 45, no. 11, 2021, doi: 10.1002/er.6891.

[53] D. Li, J. Guo, J. Zhang, L. Zhan, and M. Alizadeh, "Numerical assessment of a hybrid energy generation process and energy storage system based on alkaline fuel cell, solar energy and Stirling engine," *J Energy Storage*, vol. 39, 2021, doi: 10.1016/j.est.2021.102631.

[54] A. R. Tavakolpour-Saleh and H. Jokar, "Neural network-based control of an intelligent solar Stirling pump," *Energy*, vol. 94, 2016, doi: 10.1016/j.energy.2015.11.006.

[55] "Mitra Ardron - Natural Innovation - Innovation: SunPulse Water - solar thermal water pump." http://www.naturalinnovation.org/?id=33&alias=sunpulsewater (accessed Nov. 05, 2022).

[56] M. A. Al-Nimr and W. A. Al-Ammari, "A novel hybrid and interactive solar system consists of Stirling engine/vacuum evaporator/thermoelectric cooler for

electricity generation and water distillation," *Renew Energy*, vol. 153, pp. 1053–1066, Jun. 2020, doi: 10.1016/j.renene.2020.02.072.

[57] X. Lai, M. Yu, R. Long, Z. Liu, and W. Liu, "Clean and stable utilization of solar energy by integrating dish solar Stirling engine and salinity gradient technology," *Energy*, vol. 182, 2019, doi: 10.1016/j.energy.2019.06.082.

[58] A. M. Soliman *et al.*, "A new system design of using solar dish-hydro combined with reverse osmosis for sewage water treatment: Case study Al-Marj, Libya," *Desalination Water Treat*, vol. 193, 2020, doi: 10.5004/dwt.2020.25782.

[59] M. Mehrpooya, N. Ghadimi, M. Marefati, and S. A. Ghorbanian, "Numerical investigation of a new combined energy system includes parabolic dish solar collector, Stirling engine and thermoelectric device," *Int J Energy Res*, vol. 45, no. 11, 2021, doi: 10.1002/er.6891.

[60] D. Li, J. Guo, J. Zhang, L. Zhan, and M. Alizadeh, "Numerical assessment of a hybrid energy generation process and energy storage system based on alkaline fuel cell, solar energy and Stirling engine," *J Energy Storage*, vol. 39, 2021, doi: 10.1016/j.est.2021.102631.

[61] B. Shboul *et al.*, "Design and Techno-economic assessment of a new hybrid system of a solar dish Stirling engine instegrated with a horizontal axis wind turbine for microgrid power generation," *Energy Convers Manag*, vol. 245, p. 114587, Oct. 2021, doi: 10.1016/j.enconman.2021.114587.

[62] E. A. Bekele and V. R. Ancha, "Transient performance prediction of solar dish concentrator integrated with stirling and TEG for small scale irrigation system: A case of Ethiopia," *Heliyon*, vol. 8, no. 9, p. e10629, Sep. 2022, doi: 10.1016/j.heliyon.2022.e10629.

[63] D. Geng, J. Cui, and L. Fan, "Performance investigation of a reverse osmosis desalination system powered by solar dish-Stirling engine," *Energy Reports*, vol. 7, pp. 3844–3856, Nov. 2021, doi: 10.1016/j.egyr.2021.06.072.

[64] "Ansys Fluent | Fluid Simulation Software." https://www.ansys.com/en-in/products/fluids/ansys-fluent (accessed Apr. 27, 2023).

[65] "COMSOL Multiphysics - Wikipedia." https://en.wikipedia.org/wiki/COMSOL_Multiphysics (accessed Apr. 27, 2023).

[66] "OpenFOAM - Wikipedia." https://en.wikipedia.org/wiki/OpenFOAM (accessed Apr. 27, 2023).

[67] K. Mahkamov, "An Axisymmetric Computational Fluid Dynamics Approach to the Analysis of the Working Process of a Solar Stirling Engine," *J Sol Energy Eng*, vol. 128, no. 1, pp. 45–53, Feb. 2006, doi: 10.1115/1.2148979.

[68] J. L. Salazar and W.-L. Chen, "A computational fluid dynamics study on the heat transfer characteristics of the working cycle of a β -type Stirling engine," *Energy Convers Manag*, vol. 88, pp. 177–188, Dec. 2014, doi: 10.1016/j.enconman.2014.08.040.

[69] S. Alfarawi, R. AL-Dadah, and S. Mahmoud, "Influence of phase angle and dead volume on gamma-type Stirling engine power using CFD simulation," *Energy Convers Manag*, vol. 124, pp. 130–140, Sep. 2016, doi: 10.1016/j.enconman.2016.07.016.

[70] M. A. Mohammadi and A. Jafarian, "CFD simulation to investigate hydrodynamics of oscillating flow in a beta-type Stirling engine," *Energy*, vol. 153, pp. 287–300, Jun. 2018, doi: 10.1016/j.energy.2018.04.017.

[71] A. Abuelyamen and R. Ben-Mansour, "Energy efficiency comparison of Stirling engine types (α, β, and γ) using detailed CFD modeling," *International Journal of*

Thermal Sciences, vol. 132, pp. 411–423, Oct. 2018, doi: 10.1016/j.ijthermalsci.2018.06.026.

[72] A. Della Torre and G. Montenegro, "(PDF) CFD modeling of a Beta-type Stirling engine," doi: http://dx.doi.org/10.13140/2.1.4560.7041.

[73] W.-L. Chen, K.-L. Wong, and Y.-F. Chang, "A computational fluid dynamics study on the heat transfer characteristics of the working cycle of a low-temperature-differential γ-type Stirling engine," *Int J Heat Mass Transf*, vol. 75, pp. 145–155, Aug. 2014, doi: 10.1016/j.ijheatmasstransfer.2014.03.055.

[74] A. K. Almajri, S. Mahmoud, and R. Al-Dadah, "Modelling and parametric study of an efficient Alpha type Stirling engine performance based on 3D CFD analysis," *Energy Convers Manag*, vol. 145, pp. 93–106, Aug. 2017, doi: 10.1016/j.enconman.2017.04.073.

[75] K. Mahkamov, "Design Improvements to a Biomass Stirling Engine Using Mathematical Analysis and 3D CFD Modeling," *J Energy Resour Technol*, vol. 128, no. 3, pp. 203–215, Sep. 2006, doi: 10.1115/1.2213273.

[76] C.-H. Cheng and Y.-F. Chen, "Numerical simulation of thermal and flow fields inside a 1-kW beta-type Stirling engine," *Appl Therm Eng*, vol. 121, pp. 554–561, Jul. 2017, doi: 10.1016/j.applthermaleng.2017.04.105.

[77] G. Xiao *et al.*, "Design optimization with computational fluid dynamic analysis of β-type Stirling engine," *Appl Therm Eng*, vol. 113, pp. 87–102, Feb. 2017, doi: 10.1016/j.applthermaleng.2016.10.063.

[78] L. Kuban, J. Stempka, and A. Tyliszczak, "A 3D-CFD study of a γ-type Stirling engine," *Energy*, vol. 169, pp. 142–159, Feb. 2019, doi: 10.1016/j.energy.2018.12.009.

[79] B. C. Caetano, I. F. Lara, M. U. Borges, O. R. Sandoval, and R. M. Valle, "A novel methodology on beta-type Stirling engine simulation using CFD," *Energy Convers Manag*, vol. 184, pp. 510–520, Mar. 2019, doi: 10.1016/j.enconman.2019.01.075.

[80] S. A. El-Ghafour, M. El-Ghandour, and N. N. Mikhael, "Three-dimensional computational fluid dynamics simulation of stirling engine," *Energy Convers Manag*, vol. 180, pp. 533–549, Jan. 2019, doi: 10.1016/j.enconman.2018.10.103.

[81] C. Cheng and D. Phung, "Numerical and experimental study of a compact <scp>100-W-class β-type</scp> Stirling engine," *Int J Energy Res*, vol. 45, no. 5, pp. 6784–6799, Apr. 2021, doi: 10.1002/er.6271.

[82] W. Zhao, R. Li, H. Li, Y. Zhang, and S. Qiu, "Numerical analysis of fluid dynamics and thermodynamics in a stirling engine," *Appl Therm Eng*, vol. 189, p. 116727, May 2021, doi: 10.1016/j.applthermaleng.2021.116727.

[83] Z. Li, Y. Haramura, Y. Kato, and D. Tang, "Analysis of a high performance model Stirling engine with compact porous-sheets heat exchangers," *Energy*, vol. 64, pp. 31–43, Jan. 2014, doi: 10.1016/j.energy.2013.11.041.

[84] C. Cheng and D. Phung, "Exchanging data between computational fluid dynamic and thermodynamic models for improving numerical analysis of Stirling engines," *Energy Sci Eng*, vol. 9, no. 11, pp. 2177–2190, Nov. 2021, doi: 10.1002/ese3.965.

[85] "Ansys Fluent User's Guide," 2022. [Online]. Available: http://www.ansys.com

[86] "National Renewable Energy Laboratory (NREL) Home Page | NREL." https://www.nrel.gov/ (accessed Nov. 05, 2022).

[87] J. Tu, G. H. Yeoh, and C. Liu, "Computational fluid dynamics: A practical approach," *Computational Fluid Dynamics: A Practical Approach*, pp. 1–477, Jan. 2018.

[88] S. C. Costa, I. Barreno, M. Tutar, J. A. Esnaola, and H. Barrutia, "The thermal non-equilibrium porous media modelling for CFD study of woven wire matrix of a

Stirling regenerator," *Energy Convers Manag*, vol. 89, pp. 473–483, Jan. 2015, doi: 10.1016/J.ENCONMAN.2014.10.019.

[89] S. Ergun and A. A. Orning, "Fluid Flow through Randomly Packed Columns and Fluidized Beds," *Ind Eng Chem*, vol. 41, no. 6, pp. 1179–1184, Jun. 1949, doi: 10.1021/IE50474A011.

[90] G. Walker and V. Vasishta, "Heat-Transfer and Flow-Friction Characteristics of Dense-Mesh Wire-Screen Stirling-Cycle Regenerators," *Adv Cryog Eng*, pp. 324–332, 1971, doi: 10.1007/978-1-4757-0244-6_41.

[91] I. Barreno *et al.*, "Numerical correlation for the pressure drop in Stirling engine heat exchangers," *International Journal of Thermal Sciences*, vol. 97, pp. 68–81, Nov. 2015, doi: 10.1016/J.IJTHERMALSCI.2015.06.014.

[92] Y. Shuai, X. L. Xia, and H. P. Tan, "Radiation performance of dish solar concentrator/cavity receiver systems," *Solar Energy*, vol. 82, no. 1, pp. 13–21, Jan. 2008, doi: 10.1016/J.SOLENER.2007.06.005.

[93] M. Babaelahi and H. Sayyaadi, "Simple-II: A new numerical thermal model for predicting thermal performance of Stirling engines," *Energy*, vol. 69, pp. 873–890, May 2014, doi: 10.1016/J.ENERGY.2014.03.084.

[94] M. Babaelahi and H. Sayyaadi, "Modified PSVL: A second order model for thermal simulation of Stirling engines based on convective-polytropic heat transfer of working spaces," *Appl Therm Eng*, vol. 85, pp. 340–355, Jun. 2015, doi: 10.1016/J.APPLTHERMALENG.2015.03.018.

LIST OF PUBLICATIONS

1. **Vaibhav Singh** and Anil Kumar. "Recent Advances in Applications of Solar Dish Stirling Engine Technology". **1st International Conference on Advances in Heat Transfer and Fluid Dynamics-2022** during December 1-3, 2022, organised by Department of Mechanical Engineering, Zakhir Hussain College of Engineering & Technology, Aligarh Muslim University, Aligarh, Uttar Pradesh. **Scopus**

2. **Vaibhav Singh** and Anil Kumar. "A Review on Simulation 2D and 3D Modelling of Stirling Engine". **Propulsion and Power Research, SCI Impact factor 4.563. Status: Under Review**

Ist International conference on Advances in Heat Transfer and Fluid Dynamics
AHTFD-2022 (December 1-3, 2022) Hybrid Mode
Department of Mechanical Engineering, Z. H. College of Engineering & Technology, AMU, Aligarh

Letter of Acceptance

Date: 17.11.2022

Dear Author,

Your paper No. **AHTFD-065** has been accepted for presentation in the International conference on Advances in Heat Transfer and Fluid Dynamics (AHTFD-22) during December 1-3, 2022 at Department of Mechanical Engineering, Z.H. College of Engineering & Technology, AMU, Aligarh.

Please incorporate the comments of the Reviewer(s), if any.

The schedule of the technical sessions will be sent separately.

You are requested to complete the registration by paying the fee. Please ignore if already done.

With Regards.

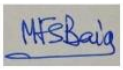

Prof. M. Faisal S. Baig
Organizing Secretary
Phone- +91-8791208584
Email: drmfbaig@yahoo.co.uk

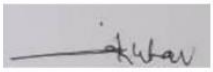

Prof. Naiem Akhtar
Organizing Secretary
Phone- +91-9457694976
Email: nakhtar.me@amu.ac.in